Monthly Notices
of the
ROYAL ASTRONOMICAL SOCIETY

MNRAS **432,** 2182–2207 (2013) doi:10.1093/mnras/stt618
Advance Access publication 2013 May 7

Star formation and dust heating in the FIR bright sources of M83

K. Foyle,[1⋆†] G. Natale,[2†] C. D. Wilson,[1] C. C. Popescu,[2,3] M. Baes,[4] G. J. Bendo,[5] M. Boquien,[6] A. Boselli,[6] A. Cooray,[7] D. Cormier,[8] I. De Looze,[4] J. Fischera,[9] O. Ł. Karczewski,[10] V. Lebouteiller,[8] S. Madden,[8] M. Pereira-Santaella,[11] M. W. L. Smith,[12] L. Spinoglio[13] and R. J. Tuffs[3]

[1]*Department of Physics & Astronomy, McMaster University, Hamilton, Ontario L8S 4M1, Canada*
[2]*Jeremiah Horrocks Institute, University of Central Lancashire, Preston PR1 2HE, UK*
[3]*Max Planck Institute für KernPhysik, Saupfercheckweg 1, D-69117 Heidelberg, Germany*
[4]*Sterrenkundig Observatorium, Universiteit Gent, Krijgslaan 281 S9, B-9000 Gent, Belgium*
[5]*UK ALMA Regional Centre Node, Jodrell Bank Centre for Astrophysics, School of Physics and Astronomy, University of Manchester, Oxford Road, Manchester M13 9PL, UK*
[6]*Aix Marseille Université, CNRS, LAM (Laboratoire d'Astrophysique de Marseille) UMR 7326, F-13388 Marseille, France*
[7]*Department of Physics & Astronomy, University of California, Irvine, CA 92697, USA*
[8]*CEA, Laboratoire AIM, Irfu/SAp, Orme des Merisiers, F-91191 Gif-sur-Yvette, France*
[9]*Canadian Institute for Theoretical Astrophysics, University of Toronto, 60 Saint George Street, Toronto, ON M5S 3H8, Canada*
[10]*Department of Physics and Astronomy, University College London, Gower Street, London WC1E 6BT, UK*
[11]*Istituto di Astrofisica e Planetologia Spaziali, INAF, Via Fosso del Cavaliere 100, I-00133 Roma, Italy*
[12]*School of Physics & Astronomy, Cardiff University, Queen Buildings, The Parade, Cardiff CF24 3A, UK*
[13]*Istituto di Fisica dello Spazio Interplanetario, INAF, Via del Fosdso del Cavaliere 100, I-00133 Roma, Italy*

Accepted 2013 March 28. Received 2013 March 28; in original form 2013 February 11

ABSTRACT

We investigate star formation and dust heating in the compact far-infrared (FIR) bright sources detected in the *Herschel* maps of M83. We use the source extraction code GETSOURCES to detect and extract sources in the FIR, as well as their photometry in the mid-infrared and Hα. By performing infrared spectral energy distribution fitting and applying an Hα-based star formation rate (SFR) calibration, we derive the dust masses and temperatures, SFRs, gas masses and star formation efficiencies (SFEs). The detected sources lie exclusively on the spiral arms and represent giant molecular associations, with gas masses and sizes of 10^6–10^8 $M_\odot$ and 200–300 pc, respectively. The inferred parameters show little to no radial dependence and there is only a weak correlation between the SFRs and gas masses, which suggests that more massive clouds are less efficient at forming stars. Dust heating is mainly due to local star formation. However, although the sources are not optically thick, the total intrinsic young stellar population luminosity can almost completely account for the dust luminosity. This suggests that other radiation sources also contribute to the dust heating and approximately compensate for the unabsorbed fraction of UV light.

Key words: galaxies: individual: M83 – galaxies: ISM – galaxies: spiral.

1 INTRODUCTION

The *Herschel Space Observatory* (Pilbratt et al. 2010) has provided us with high sensitivity and angular resolution maps of nearby galaxies in the far-infrared (FIR), which has allowed us to spatially resolve their cold dust emission. Dust plays a key role in the chemistry of the interstellar medium, acting as a catalyst for the formation of molecular gas, the fuel for star formation. However, it complicates our view of galaxies by obscuring UV and optical photons from stars and then re-radiating this light in the infrared. Thus, over a third of a galaxy's bolometric luminosity comes to us at these longer wavelengths (e.g. Bernstein, Freedman & Madore 2002; Draine 2003). In the past it has been very difficult to detect the dust emission in galaxies between 200 and 850 μm. Ground-based telescopes have lacked the sensitivity and, prior to *Herschel*, space telescopes could not make detections at these wavelengths.

Apart from the measurement of dust luminosities and masses, the maps from *Herschel*, spanning 70 to 500 μm, can be used to estimate two important quantities: the gas mass and the average

⋆E-mail: foylek@physics.mcmaster.ca
† The first two lead authors have been co-equal contributors to the majority of the work presented in this paper.

intensity of the radiation field heating dust within galaxies. In the first case, since dust is generally well mixed with gas, we can use dust mass estimates inferred by spectral energy distribution (SED) fitting as a proxy for the total gas mass, assuming a gas-to-dust ratio (GDR; e.g. Hildebrand 1983; Boselli, Lequeux & Gavazzi 2002; Eales et al. 2010, 2012). While atomic gas measurements are relatively well known due to 21 cm line measurements, molecular gas measures are more challenging since we are forced to use an alternative tracer like CO rather than directly measuring molecular hydrogen. This requires the calibration of this tracer, which is known to vary with environment, metallicity and density (e.g. Shetty et al. 2011). *Herschel* maps have been used to help spatially resolve this calibration factor (i.e. the X-factor) improving our view of the molecular gas component in galaxies (Sandstrom et al., 2012). Typically dust emission maps also have higher resolutions, at least at the shorter wavelengths, and superior sensitivity to CO maps.

Dust emission SED fitting also provides a measure of the average radiation field energy density heating the dust or, alternatively, the average dust temperature. These quantities are connected to the luminosity of the heating sources and are therefore, in principle, useful to understand which radiation sources are heating the dust. In particular, in order to use dust emission to infer star formation rates (SFRs), one would like to quantify the fraction of dust heating due to recent star formation. However, the dust can also be powered by an older stellar population (e.g. Popescu & Tuffs 2002; Bendo et al. 2012; Groves et al. 2012; Smith et al. 2012).

Herschel has improved our view of the morphological structure of the dust emission and has allowed us to better separate compact sources from diffuse emission in some of the FIR bands. We find both clumpy, compact regions associated with sites of recent star formation, detected also in Hα emission, and a smoother, more diffuse component (e.g. Verley et al. 2010). Although *Herschel* images have a resolution of 6 arcsec at the shortest wavelengths (70 μm), at longer wavelengths it increases to 36 arcsec at 500 μm. Therefore, to date most studies have been forced to degrade the high-resolution Photodetector Array Camera and Spectrometer (PACS; Poglitsch et al. 2010) maps (70 and 160 μm) in order to match them to the longer wavelength Spectral and Photometric Imaging Receiver (SPIRE; Griffin et al. 2010) data (i.e. Bendo et al. 2010, 2012; Aniano et al. 2012; Boquien et al. 2012; Smith et al. 2012). This has meant that these studies have averaged over large physical areas (i.e. pixel-by-pixel analysis at 36 arcsec resolution or azimuthal averages). Thus, the structure evident in the PACS maps is mostly lost. In this work, we attempt to capitalize on the highest resolution PACS maps, while still making use of the lower resolution SPIRE maps, in order to study the compact, clumpy regions in the FIR continuum emission. Our method relies on the multi-wavelength extraction tool, GETSOURCES (Men'shchikov et al. 2012), which allows us to preserve the native resolution of the images.

This paper uses this new technique on M83, a galaxy from the Very Nearby Galaxies Survey (PI: C. D. Wilson). The close proximity of M83 (4.5 Mpc; Thim et al. 2003) affords us high spatial resolution (130 pc at 70 μm). M83 also has a strong spiral structure and prominent bar, allowing us to investigate different regions within the galaxy.

The main goal of this work is the investigation of the properties of the compact sources detected in the FIR, in terms of gas masses, star formation and dust heating. Specifically, we address the following questions: (1) Which range of giant molecular cloud (GMC) masses are associated with the FIR compact sources in M83?; (2) How efficient is the star formation within them?; and (3) Is the local star formation the predominant radiation source powering the dust emission?

To this purpose, we developed a procedure consisting of the following steps. We use GETSOURCES to detect and extract compact regions from the FIR (70–350 μm), which we call 'clumps'. We also measure the flux in the mid-infrared (MIR; 8 and 24 μm) and Hα using the clump area and position. In all cases, a local background emission component is subtracted. For each well-detected source, the corresponding dust luminosity, dust mass, average radiation field energy density and dust temperature are determined using a two-component dust emission SED fitting method of the MIR and FIR. Using the dust mass we infer a gas mass for each source, using a constant GDR. We also derive the clump SFRs by applying the Calzetti et al. (2007) calibration on the measured Hα and 24 μm fluxes.

We structure the paper in the following sections: background and motivation (Section 2), observations and data reduction (Section 3), compact source extraction (Section 4), dust emission SED fitting (Section 5), SFRs and gas mass estimations (Section 6), and presentation of results (Section 7) and discussion (Section 8). We conclude with a summary of the main findings (Section 9).

2 BACKGROUND AND MOTIVATIONS

2.1 Gas and star formation on sub-kpc scales

During the last few years, high-resolution maps of nearby galaxies in several wavelengths including UV, IR, emission line and radio have become gradually available and opened the possibility to study the relation between gas mass surface density and star formation, known as the Schmidt–Kennicutt law (hereafter the S-K relation; Schmidt 1959; Kennicutt 1998) on scales of kpc/sub-kpc within galaxies. The S-K relation is commonly expressed as

$$\Sigma_{\rm gas} = A\,\Sigma_{\rm SFR}^{N}. \quad (1)$$

The value of the exponent N is particularly important and remains debated. $N = 1$ implies that the star formation efficiency (SFE) or gas depletion time-scale is constant, while $N > 1$ implies that the SFE is greater for high-density regions, or that the time-scale is shorter for high-density regions. While global averages across galaxies have shown that the total gas mass ($\rm H\,I + H_2$) surface density has a power-law relation with the SFR surface density (i.e. $N = 1.4$; Kennicutt 1989), spatially resolved studies of star formation have shown that the SFR surface density is more tightly coupled to the molecular gas surface density (e.g. Wong & Blitz 2002 and Bigiel et al. 2008).

Reliable measurements of SFR within galaxies can be performed by combining optical/UV and infrared flux measurements, according to calibrations such as Calzetti et al. (2007) or Zhu et al. (2008) for Hα + 24 μm and Bigiel et al. (2008) for UV + 24 μm. In these empirically based calibrations, dust emission is used to estimate the fraction of optical/UV light attenuated by dust. These calibrations are now considered the most accurate way to determine SFRs within galaxies, at least when used on galaxy regions which are bright enough (SFR $>=$0.001 $\rm M_\odot\ yr^{-1}$; Kennicutt & Evans 2012).

Spatially resolved studies of the SFR typically involve aperture photometry of the SFR tracers. The size of the aperture has been primarily dictated by the beam sizes. Typically background emission is subtracted from the SFR tracers either locally, in annuli directly surrounding the apertures, or, in the case of crowded regions, more extended zones are used (Calzetti et al. 2005). Background

subtraction is typically performed because the star formation tracers have contamination from other sources not directly associated with star formation.[1] The 24 μm emission includes cirrus emission from an older stellar population (Popescu & Tuffs 2002), which may contribute as much as 30 per cent of the emission (Kennicutt et al. 2007). Hα emission may also include diffuse ionized gas (Ferguson et al. 1996). Background subtraction has proven to have effects on the S-K relation. Subtracting a diffuse component more readily suppresses the fainter star-forming regions (Liu et al. 2011). Thus, studies that have used aperture photometry on star-forming regions and background subtraction have found a super-linear relation (e.g. Kennicutt et al. 2007). Meanwhile, pixel-by-pixel analyses that have not subtracted a diffuse component have recovered a linear relation (e.g. Bigiel et al. 2008).

The measures of star formation tracers are quite advanced due to the relatively high resolutions available, but tracing gas in extragalactic studies has proven to be more complicated. While measurements of the atomic gas component are available by using the 21 cm line emission (e.g. THINGS; Walter et al. 2008), cold molecular hydrogen has proven more challenging. Due to the low mass of the molecule, it requires high temperatures to excite the rotational transitions of molecular hydrogen. Thus, it is virtually impossible to measure the total amount of molecular hydrogen directly. Instead, an alternative tracer like CO is commonly used (Bolatto, Wolfire & Leroy 2013). Typically conversions from CO are done using a constant X-factor. However, this factor can vary considerably depending upon the metallicity, density and temperature (Kennicutt & Evans 2012). Accurate measures of the molecular component associated with star formation are particularly important, because it seems that star formation is more directly coupled to molecular gas than to total gas.

Due to the comparatively low resolution and sensitivity of the molecular gas maps, only a few studies (e.g. Rahman et al. 2011) have subtracted diffuse emission from the gas. However, diffuse gas unrelated to star formation sites is most likely present. Low-mass clouds that are unresolved will present themselves as a diffuse component and may not host star formation. Ideally, one should also account for a diffuse gas component. Furthermore, there is growing evidence that low-mass GMCs may not have a corresponding star-forming region (e.g. Hirota et al. 2011).

In light of the issues surrounding the molecular gas measures, we are motivated to capitalize on the high-resolution dust emission maps from *Herschel*. By employing a GDR we present an alternative way to probe the SFE on spatially resolved scales. Inspired by the aperture photometry studies of star-forming regions, we employ the dust maps to isolate and extract clumpy regions which are likely associated with individual or groups of molecular clouds. For both the star formation tracers and the dust, we can also subtract a diffuse background component, thus treating both the star formation and gas tracers in a similar fashion.

2.2 Dust heating within galaxies

In general, dust emission within galaxies without AGNs is powered by radiation coming from both sites of recent star formation and more evolved stellar populations. However, there is a longstanding debate about the exact fraction of dust heating contributed by each stellar population (e.g. Boquien et al. 2011; Law, Gordon & Misselt 2011; Bendo et al. 2012, for recent references), which depends on several factors: the intrinsic emission SED of the stellar populations, the dust mass and optical properties, and the relative dust–star geometry.

Recent observational works investigating the origin of the radiation heating the dust in nearby galaxies have looked for correlations between the source dust temperature (or, alternatively, FIR colour) and source stellar population luminosities, as traced by SFR for the young stars and NIR luminosity for the old stars (e.g. Boquien et al. 2011; Bendo et al. 2012; Foyle et al. 2012; Smith et al. 2012).[2]

The presence of an observed correlation of this kind has often been used as evidence that a particular stellar population is the dominant source heating the dust. Although it might seem intuitive that a higher dust temperature should correspond to a stellar population with a higher intrinsic luminosity, deducing the origin of the radiation heating the dust in this way can be potentially misleading. The reason is that the intrinsic luminosity of a stellar population and the average dust temperature are not necessarily proportional to each other, even in the case where the stellar population in question is the dominant source of dust heating.

The luminosity of a stellar population gives the amount of total radiative energy per unit time injected by a stellar population locally in the interstellar medium. Therefore, one can expect at most a proportionality between the observed dust luminosity and the intrinsic stellar population luminosity for a set of sources, provided all the sources are mainly heated locally by the same kind of stellar population and heating from radiation sources external to the areas considered is negligible.[3]

Specifically, one can express the total dust luminosity $L_{\rm dust}$ for a source as

$$L_{\rm dust} = L^{\rm int}_{\rm stars}\left(1 - {\rm e}^{-\tau}\right), \tag{2}$$

where $L^{\rm int}_{\rm stars}$ is the total intrinsic luminosity from a certain stellar population and τ is the source luminosity-weighted optical depth. The optical depth can be expressed as

$${\rm e}^{-\tau} = \frac{L^{\rm out}_{\rm stars}}{L^{\rm int}_{\rm stars}}, \tag{3}$$

where $L^{\rm out}_{\rm stars}$ is the escaping unabsorbed source stellar population luminosity. All the aforementioned luminosities are integrated over wavelength spanning the entire emission spectral range. From equation (2) one can see that, if τ has similar values for a sample of sources, a correlation between $L_{\rm dust}$ and $L^{\rm int}_{\rm stars}$ will be found. Note also that equation (2) implies that $L_{\rm dust}$ cannot exceed $L^{\rm int}_{\rm stars}$. If this is observed for a sample of sources, it would mean that the dust is significantly heated by radiation coming from another stellar population beyond that associated with $L^{\rm int}_{\rm stars}$.

In order to have a proportionality between the source intrinsic stellar luminosity and the source average dust temperature, an additional assumption is required: each of the detected sources should be associated with a similar amount of dust mass, $M_{\rm dust}$. Assuming that the dust emission can be described by a

[1] The relative amount of background emission that needs to be removed is still the subject of much debate. See e.g. Leroy et al. (2012) for a discussion on the nature of the diffuse MIR emission.

[2] The quantities typically considered are *surface densities* of SFR and NIR luminosity rather than total values. For pixel-by-pixel analyses this amounts to multiplication with a constant; thus, it does not affect the nature of the correlation with dust temperature.

[3] The latter assumption can easily break down when considering arbitrary galactic regions. For the compact FIR sources associated with star formation regions, the heating is usually thought to be dominated by the local young stellar populations but see further discussion in Section 8.3.

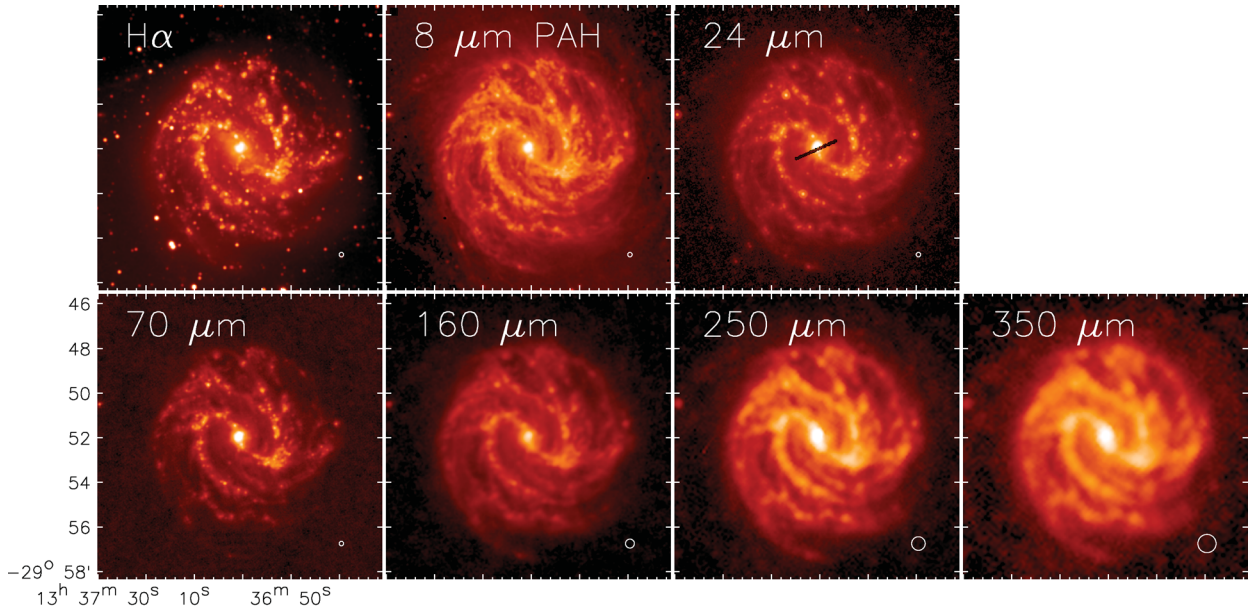

Figure 1. M83 at different wavelengths at the resolution used in this study denoted by the white circle in the bottom right of each panel. Upper row: Hα from the SINGG survey and *Spitzer* IRAC 8 and MIPS 24 μm maps. Lower row: *Herschel* 70, 160, 250 and 350 μm maps.

modified blackbody function such that $\kappa_\nu B_\nu(T_{\rm dust})$, where $\kappa_\nu \propto \nu^\beta$ is the absorption coefficient, β is the emissivity, B_ν the Planck function and $T_{\rm dust}$ the dust temperature, it can be shown that $L_{\rm dust} \propto M_{\rm dust} \int \kappa_\nu B_\nu(T_{\rm dust}){\rm d}\nu \propto M_{\rm dust} T_{\rm dust}^{4+\beta}$. By combining the latter relation with equation (2), it follows that

$$\frac{L_{\rm stars}^{\rm int}}{M_{\rm dust}} \propto \frac{T_{\rm dust}^{4+\beta}}{(1-{\rm e}^{-\tau})}. \quad (4)$$

If $M_{\rm dust}$ and τ have similar values for all the sources considered, the average intensity of the radiation heating the dust approximately scales only with the stellar luminosity and, as a consequence, the dust temperature $T_{\rm dust}$ is directly related only to $L_{\rm stars}^{\rm int}$ through equation (4). In this case, it is likely that a specific stellar population is heating the dust, if one finds that the intrinsic luminosity of that the stellar population correlates with the observed dust temperature. However, the amount of dust mass, the dust–star geometry and, therefore, the value of τ can be substantially different for each source. Thus, in general, it cannot be expected that the luminosity of a stellar population is correlated with the dust temperature, even if that the stellar population is responsible for the dust heating.

Equations (2) and (4) are almost equivalent to each other and they both express the relation between the dust luminosity and stellar population luminosity. The only difference is that $L_{\rm dust}$ in equation (2) includes all the dust and polycyclic aromatic hydrocarbon (PAH) emission throughout the entire infrared range. In equation (4), we assumed that the dust emission can be modelled by a single modified blackbody curve. This is a good approximation if one considers only the FIR region of the emission spectra. However, usually the FIR luminosity is the dominant contribution to $L_{\rm dust}$.

Thus, equation (4) can be used to probe the extent to which a given stellar population is powering the dust emission. We can do so by comparing the local, cold dust temperature with a measure of the local stellar population luminosity divided by the corresponding dust mass. As before, if the value of τ is varying in a relatively small range, a correlation between $L_{\rm stars}^{\rm int}/M_{\rm dust}$ and $T_{\rm dust}$ will be observed if the stellar population considered is responsible for heating the dust.

For example, one can use the SFR value as a tracer of the UV luminosity of the young stellar populations associated with each source. Therefore, if the radiation from young stars dominates the dust heating, the SFR/$M_{\rm dust}$ ratio is expected to be more tightly coupled to the dust temperature than the SFR alone. Thus, an observed correlation between SFR/$M_{\rm dust}$ and $T_{\rm dust}$ would suggest that star formation is powering the observed dust emission.

Given this, we are motivated to include a comparison of the measured SFR/$M_{\rm dust}$ (or, equivalently, SFE if one assumes a constant dust-to-gas mass ratio) with $T_{\rm dust}$ for the sources we detect, in addition to simply a comparison of the SFR and dust temperature, which is typically seen in the literature. The results of these comparisons are shown in Section 7 and discussed in Section 8.

3 OBSERVATIONS

In this work we use the *Herschel* FIR maps of M83 from the Very Nearby Galaxies Survey (PI: C. D. Wilson) as well as ancillary MIR and Hα maps to trace dust/PAH emission and SFR. Fig. 1 shows M83 at each of the wavebands considered.

3.1 FIR images

We use FIR images from the *Herschel Space Observatory* to trace cold dust emission. We use 70 and 160 μm maps taken with the PACS (Poglitsch et al. 2010) and 250 and 350 μm maps taken with the SPIRE (Griffin et al. 2010).[4] The PACS images are processed using both HIPE v5 and SCANAMORPHOS v8 (Roussel 2012), and the SPIRE images are processed with HIPE and BRIGADE (Smith et al. 2012). The PACS images were corrected from the v5 photometric calibration files to v6 with corrective factors of 1.119 and 1.174

[4] We performed an initial test including the 500 μm map as well, but we found that the uncertainties on the source fluxes were so large that they were not useful to constrain the source SEDs. This was caused by the low resolution of the 500 μm map (PSF FWHM = 36 arcsec). Thus, we decided not to include the 500 μm map in our analysis.

for the 70 and 160 μm maps, respectively. The SPIRE images are multiplied by 0.9828 and 0.9839 for the 250 and 350 μm maps, respectively, in order to convert from monochromatic intensities of point sources to monochromatic extended sources. The images are kept in their native resolution with a full width at half-maximum (FWHM) of the point spread function (PSF) of 6.0, 12.0, 18.2 and 24.5 arcsec for the 70, 160, 250 and 350 μm maps, respectively. For more details on how the images were processed, we refer to Bendo et al. (2012) and Foyle et al. (2012, hereafter F12).

3.2 MIR images

We trace the warm dust and PAH emission using MIR maps taken from the *Spitzer* Local Volume Legacy Survey (Dale et al. 2009). Specifically, we use the 8 and 24 μm maps from IRAC and MIPS instruments. We subtract the stellar component of the emission in the 8 μm map using a scaling of the IRAC 3.6 μm map, according to the relation provided by Helou et al. (2004): $F_\nu(8\,\mu\text{m, dust}) = F_\nu(8\,\mu\text{m}) - 0.232F_\nu(3.6\,\mu\text{m})$. In the 24 μm map, the nuclear region is saturated, so this region is excluded from our analysis. Because of reasons explained in Section 4, we degrade the resolution of the MIR maps to 6 arcsec in order to match the resolution of the 70 μm map.

3.3 Hα images

We use continuum-subtracted Hα maps from the Survey for Ionization in Neutral Gas Galaxies (SINGG; Meurer et al. 2006). We correct the Hα maps for Galactic extinction using a factor 1.167 from the NASA/IPAC Extragalactic Database that is based on Schlegel, Finkbeiner & Davis (1998). As for the MIR maps, we degrade the Hα map to a resolution of 6 arcsec matching that of the 70 μm map. We use the Hα maps in conjunction with the 24 μm MIR map, in order to measure the SFR of the extracted compact sources (discussed in greater detail in Section 6).

4 COMPACT SOURCE EXTRACTION

In order to extract compact sources in the FIR maps (70–350 μm), we use the new multi-scale, multi-wavelength tool, GETSOURCES (Men'shchikov et al. 2012). GETSOURCES is specifically designed to work with the FIR images of *Herschel*. The data from *Herschel* span a range of angular resolutions from 6.0 to 36.0 arcsec and, thus, any source extraction code must be able to handle these extremes, which poses concerns for source blending at longer wavelengths.

Rather than extracting sources directly from observed images (i.e. GAUSSCLUMP, Stutzki & Guesten 1990; CLUMPFIND, Williams, de Geus & Blitz 1994; SExtractor, Bertin & Arnouts 1996), GETSOURCES analyses spatial decompositions of the images across different scales and different wavelengths. Wavelength-independent images are generated to detect sources at each spatial scale. The original images are then used to perform photometry on the detected sources. This procedure takes into account the different angular resolutions of the maps, background subtraction and source blending. We briefly describe the key steps of the process here, but refer the reader to Men'shchikov et al. (2012) for a detailed description on how GETSOURCES extracts and measures the properties of compact sources, including a comparison with other similar codes.

After the images are aligned to the same spatial grid, GETSOURCES decomposes the original maps into single-scale detection images. This is done by using a process of successive unsharp masking, where the original images are convolved with Gaussians and subtracted successively, in order to enhance the visibility of emission on different scales. The FWHM of the Gaussians varies between twice the pixel size to a maximum of 18 times the resolution of the image or the image size. The image resolution is the only information the user needs to provide. The background and noise in the single-scale detection images are then removed by intensity thresholding. The clean single-scale detection images at each wavelength are then combined into single-scale wavelength-independent detection images, allowing for the use of all the information across all bands simultaneously for the source detection. Many detection codes rely on independent catalogues at each waveband which are then matched using an association radius, which can introduce large unknown errors. By dividing the images into single scales, this process can be avoided.

On the combined single-scale detection images, a given source will appear at a small scale and gradually get brighter until it is seen at a scale roughly the true size of the source. Beyond this, the source begins to vanish again. GETSOURCES tracks the evolution of the source through the spatial scales and creates source masks to identify the sources. The scale where the source is the brightest provides an initial estimate of the source *footprint*. A source must have a signal-to-noise ratio of at least 3σ in at least two bands in order to be considered detected. Coordinates of the sources are determined using the moments of the intensities. Once the sources have been detected in the combined images over all spatial scales, GETSOURCES performs source flux measurements on the observed images at each waveband and simultaneously subtracts a background by interpolating under the sources *footprints*. Partially overlapping sources are 'deblended' using an iterative process.

Upon completing the extraction and measurements, the user is supplied with a table giving the location and size of each source at each waveband. Due to the fact that the resolution decreases with increasing wavelength, the apparent source size increases with wavelength. The measured properties also include total flux, peak flux, degree of source blending, monochromatic and global detection significance. The detection significance at each wavelength is essentially a signal-to-noise ratio, which is determined by the ratio of the peak flux of the source to the standard deviation in an annulus surrounding the source on the detection maps. The global detection significance is determined by the square root of the sum of the squares of the detection significance at each wavelength. As discussed in the following sections, we apply a minimum threshold for the global detection significance value to remove some sources not well detected.

We now briefly describe the parameters we defined in the source extraction process.

4.1 Preparing images

We supply all images (Hα, MIR and FIR) to GETSOURCES, but only use the FIR images to detect the compact sources, since we seek to trace the location of cold compact clouds.

The images are aligned to the same grid and converted to MJy sr^{-1}, with a pixel size of 1.4 arcsec. For the SPIRE images, GETSOURCES uses the beam areas in order to convert the units from Jy $beam^{-1}$ (423 ± 3, 751 ± 4, 1587 ± 9 $arcsec^2$, for the 250, 350 and 500 μm images, respectively). The images are all aligned to the WCS of the 70 μm maps. Observational masks are created, which denote the image area over which GETSOURCES is meant to look for sources, which speeds the detection process. The alignment and masks are visually checked.

Since GETSOURCES has been designed to work with FIR *Herschel* maps, we decided to degrade the MIR and Hα maps to the angular resolution of the 70 μm map. This should reduce possible systematic effects due to the use of the program on a larger range of spatial resolutions than the one on which it has been designed and tested. Furthermore, we performed a test to examine the efficiency of GETSOURCES in recovering source fluxes at different resolutions, by running the program on a set of convolved 70 μm maps. In this test, source fluxes are expected to be the same at each resolution. We found that the accuracy of the source flux measurement decreases with poorer resolution, but the average systematic effect does not seem to be large enough to affect our results substantially (see Appendix A for more details).

4.2 Compact source measurements

The source detection has been performed using only the FIR maps, since we aimed to select sources due to their FIR brightness and not necessarily MIR and Hα counterparts. However, MIR and Hα maps have been provided to GETSOURCES for source photometry. GETSOURCES detects 186 compact sources across M83. However, in the analysis described in the following sections, we only include those sources with a detection significance above 20. Furthermore, since a high global detection significance does not necessarily imply that the photometry is accurate for each single waveband, we further removed all the sources with a photometric signal-to-noise ratio lower than 1σ in at least one band between 8 and 250 μm (that is, we occasionally retained sources detected in all bands but the 350 μm band). After this source selection, our sample is reduced to 121 sources.

Fig. 2 shows the location of all the detected sources overlaid on the 70 μm map, with colours denoting the detection significance.

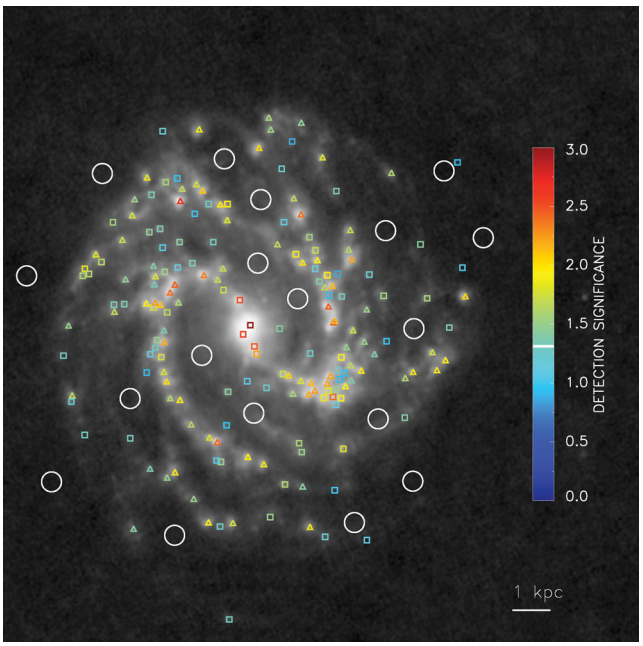

Figure 2. M83 at 70 μm with the compact source locations marked with colours corresponding to the detection significance (log 10 scale). A detection significance of 20 is used as a cut-off for retaining sources for further analysis. Sources that are used in the study are denoted with triangles and excluded sources are denoted with squares (see the text for criteria). Apertures showing the measurement locations of interarm emission are displayed in white.

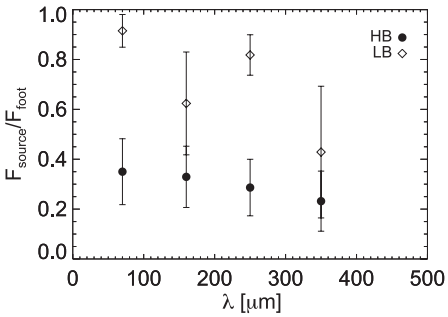

Figure 3. Median value of the ratio of the measured source flux to the total flux in the source footprint for both the high (full circles) and low (open squares) source background subtractions. At longer wavelengths, the background is greater due to the increasing size of the footprint.

Sources that are retained in the study are denoted with triangles, while sources that are excluded are denoted with squares. We note that the sources lie almost exclusively on the bar ends and the spiral arms. Very few sources are detected in the interarm regions and along the bar. This does not mean that compact sources do not exist in these regions, but rather that the sources there are not bright enough to be detected. Thus, it seems that only the bar ends and spiral arms harbour bright compact sources that we can detect.

Our spatial resolution at 70 μm allows us to measure intrinsic sources sizes only for sources having radii larger than 130 pc. We find a median radius of 150 pc at this waveband. This implies that the majority of our sources are unresolved or barely resolved. Thus, it is not possible to determine a physical radius for all the sources.

At each waveband we obtain the total flux of each of the extracted sources (hereafter $F_{\rm source,\,HB}$) and of the corresponding background emission, which has been interpolated and subtracted by GETSOURCES. Because GETSOURCES interpolates the background from regions very close to the sources, this background measurement is actually determined in the vicinity of the spiral arms. We find that the background makes up more than 50 per cent of the flux in the footprint. Fig. 3 shows the relative flux of the source to the total flux in the footprint. The relative fraction decreases with wavelength mainly because, due to the poorer resolution at longer wavelengths, the footprint size increases and thus a relatively larger amount of background flux is included in the footprint. However, part of this relative flux variation might be also due to an intrinsic higher fraction of diffuse background emission at longer wavelengths. We find that at all wavelengths the source makes up less than 50 per cent of the emission in the footprint. For this reason, we refer to this way of performing the source photometry as 'high-background' (HB) source flux measurement. In order to identify possible systematic uncertainties due to the way the background is subtracted, we also consider an alternative measure for the background, estimated in the interarm regions, as shown in the next subsection.

4.3 Low-background source flux measurement

The background estimated by GETSOURCES is basically a measure of the smooth emission component associated mainly with the spiral arms. However, typically the photometry of star-forming regions is done by subtracting an average brightness measured in the interarm regions close to the sources (i.e. Calzetti et al. 2007; Liu et al. 2011) and, as said before, it is important to check if there are substantial differences on the final results if the background measurement is performed differently.

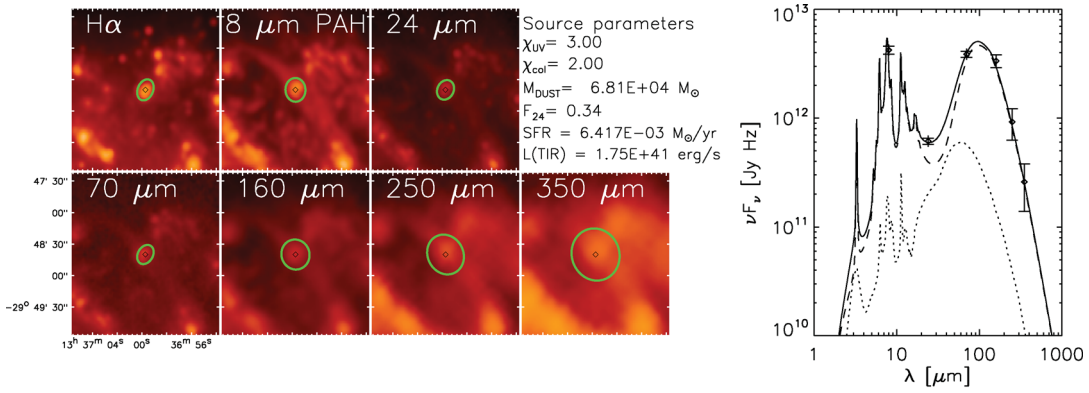

Figure 4. Example of source flux measurement and SED fitting. The maps on the left show a small area of the disc of M83 around one of the detected sources. The ellipses overplotted on each map delineate the source footprint determined by GETSOURCES. On the right, we show the two-component SED fit of the same source with the best-fitting parameter and SFR values listed aside. The dashed and the dotted line represent the diffuse dust emission component and the PDR emission component, respectively.

For these reasons, we decided to perform aperture photometry in several interarm regions selected by eye (see Fig. 2). Specifically, we selected 18 interarm regions, which are all sufficiently far away from the detected sources at all wavelengths. The diameter size of the apertures is 25 arcsec which is large enough to obtain a good estimate of the rather uniform interarm emission. For each aperture we measured the average surface brightness with an uncertainty derived from the standard deviation of the surface brightness within each aperture and the flux calibration uncertainty.

Once we obtained the flux measurements for the interarm apertures, we performed a 'low-background' (LB) source flux measurement in the following way: for each source, we consider the flux in the full footprint determined by GETSOURCES and subtract the interarm surface brightness, estimated from the aperture that is closest to the source, multiplied by the area of the source footprint (typically, the distance between the centres of each source and the closest interarm region is about 1 kpc or less).[5] Since the GETSOURCES background is usually larger than that determined in the interarm region, in general the LB source fluxes are higher than the HB ones. Fig. 3 shows that the LB measurements have higher fluxes relative to their background at all wavelengths than HB flux measurements.

5 SED FITTING

In the absence of a strong contribution from AGNs, the galaxy dust/PAH emission SED on sub-kpc/kpc scales can be modelled as the sum of two emission components: a warm component largely emitting in the MIR, produced by dust in photodissociation regions (PDRs) and heated predominantly by young stellar populations, and a diffuse emitting component, emitting mostly in the FIR and MIR PAH line emission, which can be powered both by older stellar populations and by the fraction of UV photons escaping from PDRs. This concept is at the base of the SED fitting method developed by Natale et al. (2010, hereafter NA10), which we used in this work to fit all the well-detected source emission SEDs derived in Section 4. In the following, we explain the main features of this SED fitting method, together with minor updates, and its application to our data set. We refer the reader to NA10 for additional details.

Using the mentioned fitting method, each observed source dust emission SED is fitted by combining two infrared SED components (see Fig. 4). The first component is a PDR SED template which has been selected by Popescu et al. (2011) among the models of Groves et al. (2008) because it provides a good fit to the dust emission from Milky Way star formation regions (specifically the chosen model is for compactness parameter $\log(C) = 6.5$, solar metallicity and hydrogen column density $\log(N) = 22$, see section 2.8 of Popescu et al. 2011 for more details). The second component, suitable to fit the diffuse dust emission, is taken from a grid of uniformly heated dust emission templates, obtained by using the dust emission code of Fischera & Dopita (2008). The diffuse dust emission is calculated assuming a Milky Way dust +PAH composition (exact dust model parameters can be found in table 2 of Fischera & Dopita 2008) and taking into account the stochastic heating of grains following the method of Guhathakurta & Draine (1989), combined with the stepwise analytical solution of Voit (1991). Since we assumed a fixed dust/PAH composition, each element of the grid is determined only by the parameters of the radiation field heating the dust. The adopted spectral shape of the radiation field is the classical Mathis, Mezger & Panagia (1983) profile, which was derived for the local interstellar radiation field, scaled by two linear factors: $\chi_{\rm UV}$, which multiplies the whole curve, and $\chi_{\rm col}$, which multiplies only the optical part of the Mathis spectra (see appendix B.2 of NA10). Therefore, $\chi_{\rm UV}$ can be seen as the intensity of the UV radiation field and $\chi_{\rm col}$ as the optical-to-UV ratio in the units of the Mathis et al. (1983) profile.

Compared to NA10, we extended the size of the grid of the diffuse dust templates, in order to cover a larger range of possible radiation field parameters. Specifically, $\chi_{\rm UV}$ and $\chi_{\rm col}$ are both allowed to vary between 0.1 and 10, a range which is reasonably large to include all the plausible values of the diffuse radiation field intensity and colour within galaxies (note that even higher radiation fields and, therefore, warmer dust are associated with the PDR component in our SED fitting procedure). We also point out that there is a degeneracy between $\chi_{\rm col}$ and the relative abundance of PAH and solid dust grains, in the sense that they both affect the 8 μm/FIR ratio (see section B.2 of NA10).

One of the main differences between our dust emission models and those of Draine & Li (2007) is that in their models the PAH abundance is varied but the optical/UV intensity ratio is fixed to

[5] We note that there are variety of possible approaches for subtracting background emission. Here we contrast two techniques, one which utilizes an interpolation scheme in the vicinity of the source and one that relies on a more distant estimate in the interarm regions.

the Mathis et al. (1983) value. Therefore, this should be taken into account when considering results involving the $\chi_{\rm col}$ parameter.

We performed a χ^2 minimization fitting of the data with the two dust emission components by varying four free parameters: $\chi_{\rm UV}$ and $\chi_{\rm col}$, the radiation field parameters defined above; $M_{\rm d}$, the dust mass of the diffuse dust component; F_{24}, the fraction of 24 μm emission provided by the PDR component. For each pair of $\chi_{\rm UV}$ and $\chi_{\rm col}$ values, the parameters F_{24} and $M_{\rm dust}$ correspond to linear scaling factors for the amplitudes of the PDR template and the diffuse dust component, respectively. The fit takes into account colour corrections calculated for each SED template following the conventions adopted for each instrument (see also section 5 of NA10 for details and the *Spitzer* and *Herschel* observer manuals for the colour correction definitions).

The uncertainties on each parameter are calculated by analysing the variation of χ^2 around the minimum found by the fitting procedure. The one sigma interval is defined as the minimum variation of a given fitting parameter around its best-fitting value, which produces a variation $\Delta\chi^2 = \chi^2 - \chi^2_{\rm min}$ always higher than 1, independently of all the possible values of the other fitting parameters. The program checks also if 'islands' of low χ^2 values (such that $\Delta\chi^2 < 1$) are present, which are detached from the region where the minimum of χ^2 has been found. In that case, a conservative uncertainty covering all the regions of low χ^2 values is provided for the fitting parameter.

Apart from the fitting parameters, our SED fitting procedure provides the total dust emission luminosity and the luminosities of each SED component. However, in contrast to blackbody fits, our method does not provide a single average dust temperature, since the output total spectra of the dust emission code are determined by probability distributions of dust temperatures, which are different for each dust grain size and composition. Furthermore, in principle different combinations of UV and optical radiation field energy densities can cause the dust to have approximately the same average cold dust temperature (that is, similar FIR peak wavelength), which would not be immediately evident by comparing different pairs of $\chi_{\rm UV}$ and $\chi_{\rm col}$ values. However, for the purposes of comparisons with other works that have relied on blackbody fits, it is useful to quote an average dust temperature. Taking advantage of the fact that the cold FIR part of the diffuse dust emission component ($\lambda > 70$ μm) can be well fitted with a modified blackbody curve with a dust emissivity index of $\beta = 2$ (consistent with observational results, i.e. F12, Davies et al. 2012; Auld et al. 2013), it is straightforward to associate with each diffuse dust template the dust temperature of the modified blackbody which best reproduces its FIR part. We will refer to this cold dust temperature as $T_{\rm dust}$. In Appendix B, we compare the dust masses and temperatures found using the SED fitting method outlined here to those determined directly from a modified blackbody function fit to the FIR wavelengths.

6 SFRS AND GAS MASSES

Although the sources are detected in the FIR bands, measurements of the flux in the source footprint in the Hα and MIR maps are also made. Hα and 24 μm emission can be used in conjunction to trace recent star formation – both unobscured and obscured (Calzetti et al. 2007). GETSOURCES also interpolates and subtracts a background for these images as well. A visual comparison of the source measurements in Hα confirmed that the source footprints are centred on bright emission peaks. In this way, we feel confident that the flux measured in the footprints is directly related to an active star-forming region.

For each source, we combined the fluxes measured in Hα and 24 μm emission to derive an SFR by using the calibration of Calzetti et al. (2007):

$$\mathrm{SFR}[\mathrm{M}_\odot\ \mathrm{yr}^{-1}] = 5.3 \times 10^{-42}(L(\mathrm{H}\alpha) + 0.031L(24\,\mu\mathrm{m})). \quad (5)$$

There are two key differences between our SFR and that derived by Calzetti et al. (2007). We detect the compact sources in the FIR maps rather than the Hα. This means we essentially estimate the SFR in the region of an FIR compact source. However, a visual check shows that almost all sources in the FIR are also present in Hα. A second difference is related to how the background is treated. Here, we rely on the background subtraction performed by GETSOURCES. This background is interpolated in the region surrounding the sources and takes into consideration neighbouring sources and deblending. In Calzetti et al. (2007), the background is determined in 12 rectangular regions surrounding sources. These regions cover a large number of pixels and extend well beyond the local neighbourhood of the sources. The mode of these regions is then used as a measure of the background. Our method produces a more 'local' background, which is greater than that which would be found by using the same method of Calzetti et al. (2007). In order to check the effect of choosing a different background level, we also determine source SFRs by using the Hα and 24 μm emission in the total source footprint, after subtraction of the background estimated from the nearest interarm aperture. This is exactly the same approach as for the LB measure for the compact source dust emission.

We note a potential problem with the SFR as outlined above. During the source extraction, it is not known what sizes the sources will potentially have. The size of the region plays an important role in deciding whether the calibration described above can be used. Regions which are too small may have SFRs which are too low. It is known that SFRs below $\approx$0.001 $\mathrm{M}_\odot\ \mathrm{yr}^{-1}$ can be problematic because there may be incomplete sampling of the initial mass function (IMF) and the assumption of continuous star formation in the last few Myr may not be valid (Kennicutt & Evans 2012; Leroy et al. 2012). Furthermore, the adopted calibration assumes that all the ionizing photons are absorbed by the gas in the H II regions. However, a fraction of ionizing photons could escape the star formation regions before ionizing the gas or, instead, could be absorbed by dust (see e.g. Boselli et al. 2009; Calzetti 2012; Relaño et al. 2012). Due to all these concerns, it is useful to consider the SFR measured in this process as a 'corrected' Hα luminosity. Whether this luminosity can accurately trace the SFR will depend on the source size and the value of the SFR.

We estimate the source gas masses $M_{\rm gas}$ by making use of the fact that the dust mass can be used as a proxy for the total gas mass (both molecular and atomic), provided one can translate the dust mass with a constant GDR to a gas mass. Dust mass is known to be better correlated with the total gas mass than with the atomic or molecular component alone (i.e. Corbelli et al. 2012).

We assume a constant GDR of 100 for the compact regions. While there is some evidence that the GDR may vary within galaxies (e.g. Sandstrom et al. 2012), particularly with metallicity, given that our sources lie almost exclusively along the spiral arms, it is not obvious that a varying GDR should be used for these sources. For example, the metallicity values for M83 are based on azimuthal averages, which include interarm regions. Thus, employing a varying GDR based on metallicity values would require introducing another assumption, namely that the GDR depends more on radius than arm and interarm regions. In the pixel-by-pixel analysis of F12, the GDR was found to be relatively constant on the spiral arms ($\approx$100) and, in contrast to the interarm regions, declined only slightly with radius

within the inner regions of the spiral arm having a GDR of 130 and the outer tips of the spiral arm having a GDR of 120. Given the current uncertainties and possible systematic effects, we simply adopt a value of 100, which is in the range found by F12 (mean value of 84 and standard deviation of 40).

By combining the SFR and gas mass measurement for each source, we estimate the star formation efficiency defined as SFE = SFR/$M_{\rm gas}$ for both types of compact source flux measurement. We stress that this SFE is different from that presented in other works (Leroy et al. 2008; Bigiel et al. 2008, etc.) which describe the SFE using only the molecular gas component. However, it is likely that the dust is mostly tracing molecular gas in these regions. M83 is known to be a galaxy with a dominant molecular component and, over the region we consider, the molecular gas constitutes 80 per cent of the total gas (Crosthwaite et al. 2002). F12 found that on the spiral arms, where most sources lie, the molecular gas component has column densities of the order of 100 $M_\odot$ pc^{-2}, whereas the atomic gas had column densities of less than 10 $M_\odot$ pc^{-2}.

7 RESULTS

Upon completing the SED fitting, as described in Section 5, we further remove sources that have high (total) χ^2 values, that is $\chi^2 > 10$, or have a dust mass uncertainty greater than a factor of 2. In the first case, we remove all the sources which are not well fitted by our model (mainly because the observed SED shape is too irregular to be fitted with our two-component model), while in the second we remove those sources with flux uncertainties that are too large at some wavebands and, therefore, cause the fitting parameters not to be constrained within small ranges. After applying this selection criteria, we are left with 90 sources. Appendix presents tables of the extracted flux and SED fitting parameters for both the HB and LB source measurements. In this section, we present the results for this set of sources. Specifically, we describe the distributions of the inferred source parameters in Section 7.1, their radial variation in Section 7.2 and their interdependence in Section 7.3.

7.1 Inferred source parameter distributions

In order to show the distributions of inferred parameters and compare them for the two types of source flux measurements, we created box and whisker plots which are shown in Fig. 5–7. The solid line in the boxes shows the median value and the box delineates the 25th and 75th quartiles. The lines extend to either the maximum and minimum values or to 1.5 times the 75th and 25th quartiles.

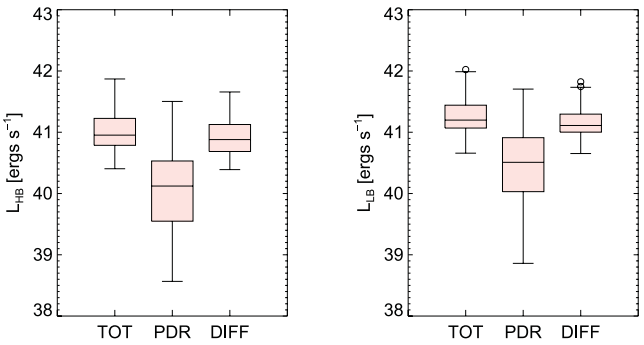

Figure 6. Box and whisker plots showing the distribution of luminosities for the sources in the HB (left) and LB (right) subtractions. We show the distributions of the total luminosity, PDR luminosity component and total diffuse component. See Fig. 5 for details.

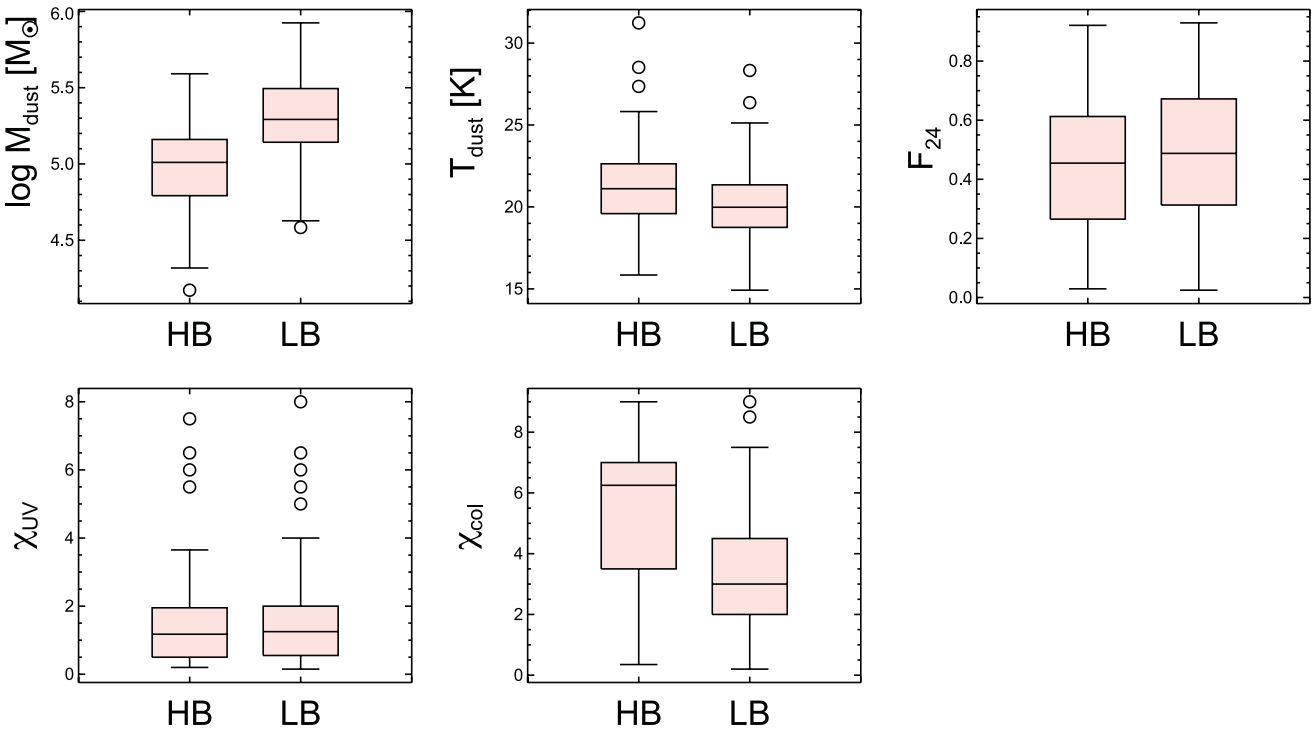

Figure 5. Box and whisker plots showing the distribution of values for the compact source dust mass (top left), temperature (top middle), F_{24} (top left)), $\chi_{\rm UV}$ (bottom right) and $\chi_{\rm col}$ (bottom middle). In each panel, the source measurements with HB (left) and LB (right) subtractions are shown. The solid horizontal line denotes the median value with the box delineating the 25th and 75th quartile range. The lines extend to the maxima and minima with open circles marking outliers (see the text).

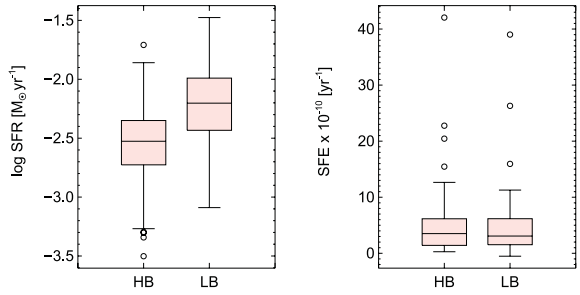

Figure 7. Box and whisker plots showing the distribution of values for the SFR (left) and SFE (right). In each panel, the source measurements with HB (left) and LB (right) subtractions are shown. See Fig. 5 for details.

If there are values beyond the latter range, they are denoted with open circles. In the following, we describe in detail the distributions for each set of parameters, that is, the SED fitting parameters, the source luminosities and the SFRs and efficiencies.

7.1.1 SED fitting parameters

As explained in Section 5, the SED fitting has four free parameters $\chi_{\rm UV}$, $\chi_{\rm col}$, $M_{\rm dust}$ and F_{24}. The box and whisker plots of these parameters and of the dust temperature are shown in Fig. 5.

The $\chi_{\rm UV}$ values (see the bottom-left panel), representing the UV radiation energy density in the units of the Mathis et al. (1983) profile (hereafter the MMP profile), show a similar distribution for both types of source measurements with most values between 0.1 and 2. Therefore, the average UV radiation field energy density of the sources seems to be typically from a few tenth up to a factor of 2 of the intensity of the local Milky Way interstellar radiation field, as described by the MMP curve.

The bottom-right panel shows the distribution of $\chi_{\rm col}$. As explained in Section 5, $\chi_{\rm col}$ expresses the ratio of the optical to UV radiation field energy density (relative to the standard MMP curve). Here the two measurements show some differences with the HB source measurement showing higher values and a greater range. This could mean that the average optical/UV ratio needed to fit the source emission is higher when one subtracts the higher GETSOURCES background. Alternatively, this could mean that the PAH abundance required for the HB fit is lower than for the LB fit (because of the $\chi_{\rm col}$–PAH abundance degeneracy described in Section 5). In other words, a lower fraction of 8 μm emission relative to the FIR emission is removed by the background estimated in the interarm apertures.

As explained in Section 5, the cold dust temperature is not fitted in our SED fitting procedure but is determined by the values of both $\chi_{\rm UV}$ and $\chi_{\rm col}$. Both source measurements show similar temperature ranges (see the top-middle panel of Fig. 5), with the HB measurement only slightly higher (about 1 K higher).

The source dust masses are shown in the upper-left panel. In both cases, the compact sources have a quite narrow range in dust masses peaking close to 10^5 $M_\odot$ and with most values between 10^4 and 10^6 $M_\odot$. The small range of masses is likely due to our resolving power, which prevents us from detecting fainter sources which tend to also have smaller dust masses. The LB measurements for the sources have higher masses, because the background determined in the interarm aperture subtracts less flux than the GETSOURCES background.

The distribution of F_{24}, the relative amount of 24 μm emission associated with PDR, is shown in the top-right panel. Both source measurements show relatively similar values, mainly in the range 0.25–0.6, which suggests that a substantial part of the 24 μm emission is contributed by stochastically heated small grains in the diffuse dust component. However, we note that PDR SED dust emission spectra can vary substantially (Groves et al. 2008) and might not be accurately reproduced by our PDR template for each individual case.

7.1.2 Source luminosities

The SED fitting procedure also provides us with a measure of the total infrared luminosity of the sources as well as the luminosities due to the PDR and the diffuse dust emission component. Fig. 6 shows the distribution of the inferred luminosity values for each component. The total luminosity values are found in a rather small interval around 10^{41} erg s^{-1}. This is likely due to the detection technique. We find that GETSOURCES does not detect sources below a minimum dust infrared luminosity of $\approx 0.5 \times 10^{41}$ erg s^{-1}. Since there are not many sources with dust luminosities higher than a few times 10^{41} erg s^{-1}, the inferred dust luminosity range covered is rather small and this has important consequences on the inferred range of SED fitted parameters and SFR values (see the discussion in Section 8). Fig. 6 also shows that the diffuse dust emission component dominates the dust luminosity. We point out that this does not necessarily mean that the dust heating from star-forming regions is not responsible for most of the dust emission, since the diffuse dust emission component can be powered by both radiation from older stellar populations and the fraction of UV photons escaping from PDRs. The origin of the dust heating will be further discussed in Section 8.3.

7.1.3 SFRs and SFEs

Fig. 7 shows the distribution of the SFR and SFE inferred values. Due to the small areas considered here (i.e. average radius of sources is 150 pc), the SFRs are quite low. As outlined in Section 6, if the SFRs are too low (i.e. below 0.001 $M_\odot$ yr^{-1}), then the calibration of Hα and 24 μm fluxes may not adequately trace the SFR. However, the majority of the sources have SFRs above this value, and furthermore, we have restricted ourselves to regions associated with recent star formation. These regions should have a good correspondence between gas and star formation. We note that the Hα contribution represents half or slightly more than half of the SFR for the sources. The median ratio of the Hα luminosity, L(Hα), to the scaled 24 μm luminosity, $0.031L(24\,\mu{\rm m})$, is 1.4.

The SFEs of the source measurements have median values with median deviation values of $3.57 \pm 3.45 \times 10^{-10}$ and $3.1 \pm 3.1 \times 10^{-10}$ yr^{-1} in the case of the HB and LB measurement, respectively. This is consistent with the findings of Leroy et al. (2008), who found that in terms of molecular gas, the SFE has a mean value of $5.25 \pm 2.5 \times 10^{-10}$ yr^{-1}.

The LB and HB measurements show considerable differences between the inferred SFR and source gas masses, with the LB measurements having higher values in both cases. However, the LB and HB measurements show roughly the same range of SFE values. This means that roughly the same relative amount of background is being subtracted for both the SFR tracers and dust emission. This suggests the amount of background subtraction does not affect the results of the SFE, provided the same technique is used for both the gas and SFR tracers.

7.2 Radial variations

We now turn to the radial variations of the SED fitting parameters, the SFR and SFE and of the dust luminosities. Previous works which have used azimuthal averages (e.g. Muñoz-Mateos et al. 2009; Engelbracht et al. 2010; Pohlen et al. 2010; Boquien et al. 2011) have found that the parameters describing the dust, including temperature and surface mass density, and the SFR tend to decrease with radius particularly for late-type spirals. These studies have averaged over both the compact regions and the more diffuse emission. By separating the compact regions, we can better disentangle how and if the radial position affects the dust properties of these sources.

In order to determine the deprojected radial position, we assume an inclination and position angle for M83 of 24° and 225°, respectively (Tilanus & Allen 1993).

7.2.1 Source infrared luminosities

Fig. 8 shows how the luminosity of the sources (upper panels) and the relative fraction of PDR and diffuse dust emission luminosity (lower panels) vary with radius. In the upper-left corner we list the Spearman rank correlation coefficient for the correlation between the luminosity components and radius. The values of the correlation coefficient approaching +1 or −1 reflect stronger correlations or anticorrelations, respectively. Values close to or less than 0.5 represent mild or weak correlations. In both the HB and LB measurements, we find only a mild correlation between the source luminosities and radius. The source luminosities show a slight decrease with radial position with scatter. We also note that the regions with the highest PDR luminosity fraction are found in the inner regions, at a radial distance of 2–3 kpc from the galaxy centre (roughly the end of the bar). However, the diffuse dust component dominates the emission for all the sources, except in a few cases.

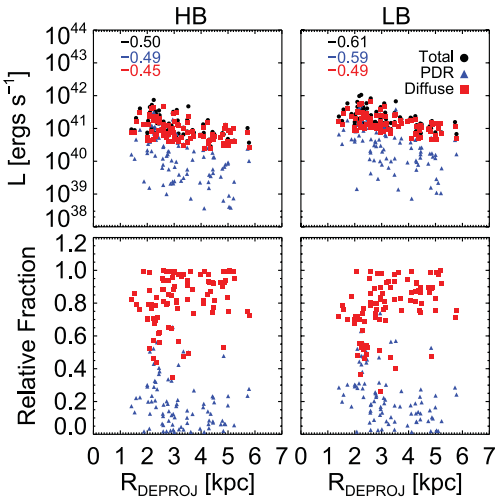

Figure 8. The radial variation of the luminosity components including the total (black circles), PDR component (blue triangles) and diffuse component (red squares), for the compact sources with HB subtraction (left) and LB subtraction (right). In the upper-left corner, we list the Spearman rank correlation coefficient for each component and radius. The relative fraction of the PDR component to the total (blue triangles) and that of the diffuse component to the total (red squares) are shown in the bottom panel for both cases.

7.2.2 Radial variations of the SED fitting parameters, SFR and SFE

Figs 9 and 10 show the SED fitting parameters and the SFR and SFE values plotted versus the source deprojected radial positions for both the flux measurements of the compact sources. The median uncertainties of the individual measurements are shown by the red error bars, and the Spearman rank coefficient is listed in the upper right of each panel.

For both the HB and LB measurements, we find little to no variations with radius for any of the SED parameters including dust mass, temperature, F_{24}, χ_{UV} and χ_{col}. There is a slight trend showing that the SFR decreases with radius, but this is far less than what is typically seen in studies on late-type spiral galaxies that employ azimuthal averages. It seems that the properties of the compact regions are quite uniform and do not vary much with location in the galaxy. This is perhaps not too surprising, since our source sample covers only a relatively small range of dust luminosities, as shown in Section 7.1. Therefore, the sources we consider likely represent similar types of objects. Although the low spatial resolution did not allow us to detect a larger range of source luminosities, it is striking that the detectable bright sources lie almost exclusively on the spiral arms or at the ends of the bar in M83, which means that the local environment may in fact be quite similar as well. This suggests that azimuthal averages of dust properties could well mask important differences in environment within an azimuthal bin. The radial decreases that are typically seen in other galaxies and for M83 in F12 using azimuthal averages might simply reflect the increasing contribution of the interarm regions at larger radii. We note, however, that the SFE is quite constant with radius. This finding is consistent with studies that use azimuthal averages and

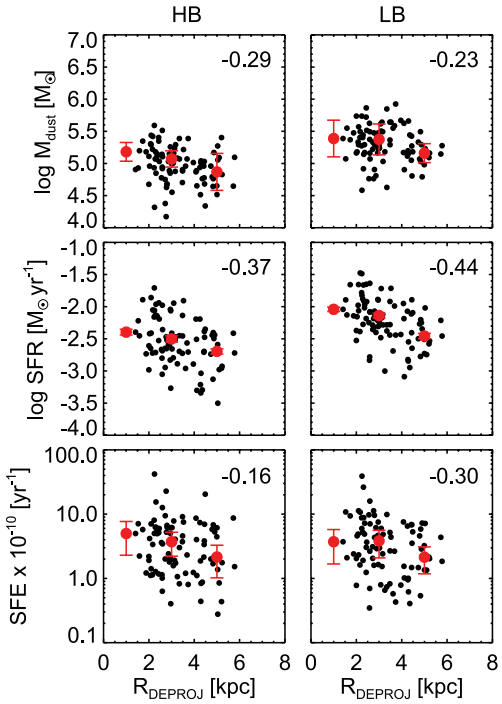

Figure 9. The radial variation of the mass, SFR and SFE for the two compact source measures. The upper-right corner lists the Spearman rank correlation coefficient. The error bars in red denote the median uncertainties of the points in three bins in the ranges 0–2, 2–4 and 4–6 kpc.

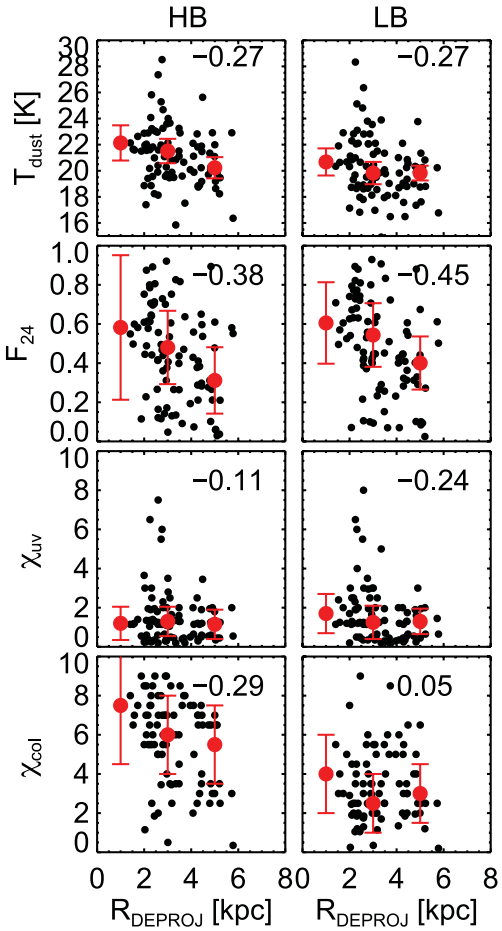

Figure 10. The radial variation of $\chi_{\rm col}$, $\chi_{\rm UV}$, F_{24} and temperature for the two compact source measures. The upper-right corner lists the Spearman rank correlation coefficient. The error bars in red denote the median uncertainties of the individual measurements in three bins in the ranges 0–2, 2–4 and 4–6 kpc.

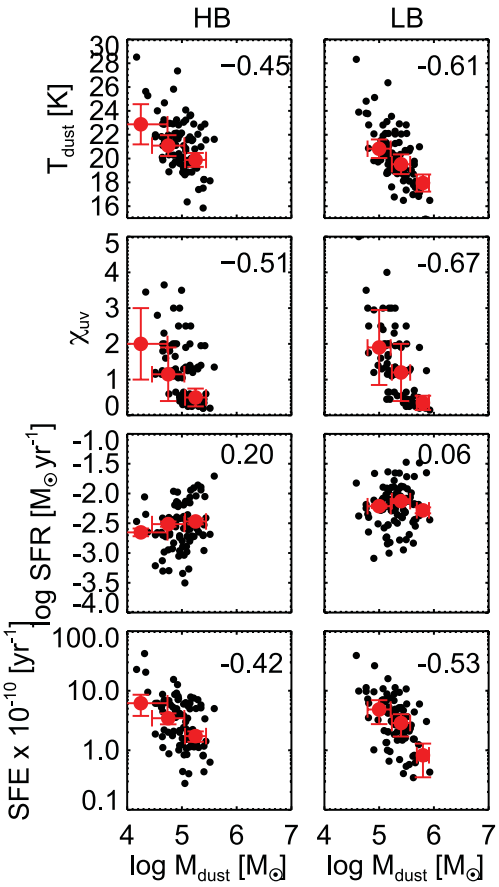

Figure 11. Correlation plots showing dust temperature, $\chi_{\rm UV}$, SFR and SFE versus dust mass for the HB (left) and LB source flux measurements (right). The Spearman rank coefficient is shown in the upper right of each panel. The red uncertainties show the median uncertainties in bins of $10^{0.4}$ $M_{\odot}$.

pixel-by-pixel analyses (e.g. Leroy et al. 2008; Blanc et al. 2009; Foyle et al. 2010; Bigiel et al. 2011).

7.3 Correlations between source properties

Having seen how the dust and star formation parameters of the compact sources vary with radius, we now turn to how they are inter-related and what types of correlations may exist between some of these parameters. In particular, we examine how the source dust mass and temperature are related to the radiation field parameters $\chi_{\rm UV}$ and $\chi_{\rm col}$ and with the SFR and efficiency. Fig. 11 shows the dust temperature, $\chi_{\rm UV}$, SFR and SFE plotted versus the dust mass, while Fig. 12 shows $\chi_{\rm UV}$, $\chi_{\rm col}$, SFR and SFE values plotted against the dust temperature.[6] As before, the red bars show the median uncertainties in equally spaced bins and the Spearman correlation coefficients are shown in the upper left of each panel. In general, we find that both LB and HB measurements of the compact sources present quite similar results.

We observe a strong correlation of $\chi_{\rm UV}$ with the dust temperature, while the optical–UV intensity ratio $\chi_{\rm col}$ is not as strongly correlated to the dust temperature measured for the sources. These findings reflect the fact the UV radiation field intensity is the fundamental parameter that determines the average dust temperature, while the optical–UV intensity ratio varies randomly among sources having same average dust temperatures. We point out that this does not mean that optical photons are not an important source of dust heating. Actually, the optical part of the radiation field accounts for more than 50 per cent of the dust heating for the diffuse dust SED component when $\chi_{\rm col} > 1$.

The upper-left panel of Fig. 11 reveals a mild anticorrelation between the dust temperature and mass for the sources. The typical error bars are much smaller than the inferred range of dust mass and dust temperature. Thus, this anticorrelation cannot be explained by the uncertain determination of dust temperature and mass, which are connected in the SED fitting since approximately $L_{\rm dust} \propto M_{\rm dust} T_{\rm dust}^{4+\beta}$. Therefore, we are confident that the sources with higher dust masses tend to have lower dust temperatures in the sample we considered. Given the strong correlation between $\chi_{\rm UV}$ and temperature, we also find an anticorrelation between $\chi_{\rm UV}$ and dust mass in the second row from the top in Fig. 11. We will discuss the significance of the dust mass–dust temperature anticorrelation in Section 8.3.

Fig. 11 (third row, left) shows that for both measures of the compact sources, the dust mass is only weakly correlated with the SFR. If the dust traces gas, this plot should be similar to the S-K relation (Kennicutt 1998), except that typically surface densities are

[6] In Appendix C, we present how these parameters vary as a function of colour.

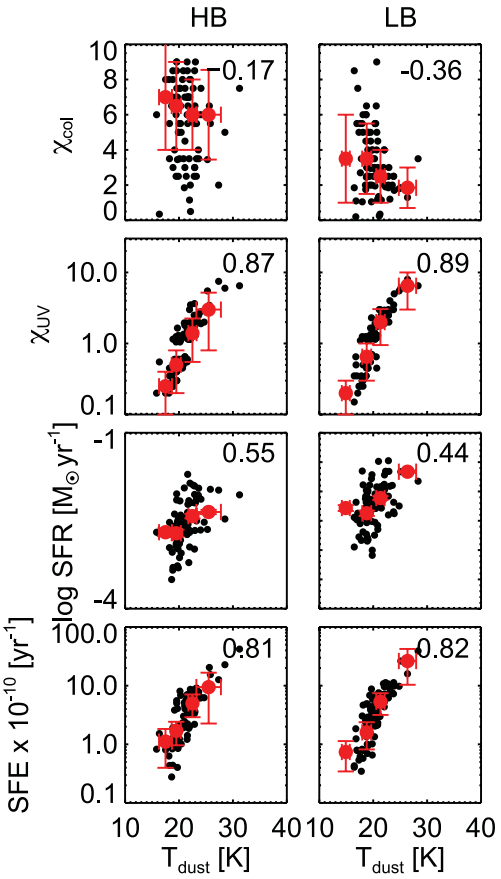

Figure 12. Correlation plots showing χ_{col}, χ_{UV}, the SFR and SFE versus dust temperature for the HB (left) and LB source flux measurement (right). The Spearman rank coefficient is shown in the upper right of each panel. The red uncertainties show the median uncertainties in bins of 2 K.

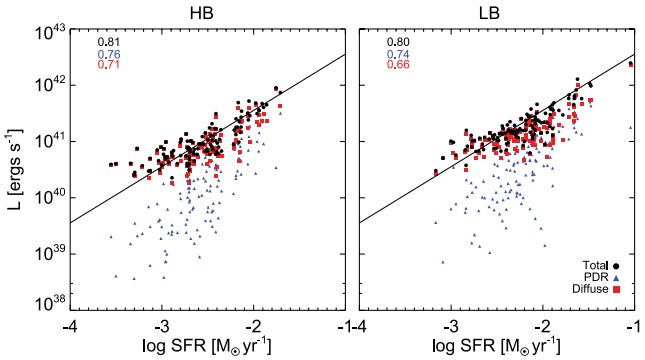

Figure 13. Dust luminosity versus the SFR for both measures of compact sources including the total luminosity (black circles), PDR component (blue triangles) and diffuse component (red squares). The correlation coefficients for each component are shown in the upper right. The solid line denotes the relation SFR $= 2.8 \times 10^{-44} \times L_{dust}$ (Calzetti 2012), which assumes that all the young stellar luminosity is absorbed and re-emitted by dust.

plotted rather than total values. The S-K relation for nearby galaxies typically shows a tight correlation between gas surface densities and the SFR surface densities, at least when the scales considered are large enough (e.g. Bigiel et al. 2008; Schruba et al. 2010, see other references in Section 2.1). The relatively constant SFR with mass suggests that more massive sources are less efficient at forming stars and will be further discussed in Section 8.2. We also find that for both measures of the compact sources, the SFR is only mildly correlated with the dust temperature (see the third row of Fig. 12). This is not unexpected since, as explained in Section 2.2, the SFR is connected to the dust temperature through the dust mass and the total luminosity-weighted optical depth.

In contrast to the lack of correlations for the SFR, we find a mild and strong correlation, respectively, of dust mass and dust temperature with the SFE. While the SFE was roughly constant with radius, we find that the SFE is anticorrelated with dust mass and correlated with dust temperature. These findings have not been seen before, as most studies have found that the SFE does not vary much with other properties in terms of pixel-by-pixel and azimuthal averages (i.e. Leroy et al. 2008). This will be further discussed in Sections 8.2 and 8.3. We note that that the anticorrelation between the SFE and mass is primarily due to the fact that the SFR does not vary much with the inferred gas mass. Thus, the correlated axes produce the anticorrelation. To check this, we performed Monte Carlo simulation assuming that the SFR was roughly constant with a Gaussian distribution and a mean and standard deviation equivalent to that found in our measurements. We assumed a similar distribution for the simulated source masses. The simulation naturally produced a linear plot of SFE versus mass with a slope of -1.05 ± 0.15. The compact sources in our analysis produced a relation with a slope of -0.71 ± 0.14. The slopes, while not identical within the uncertainties, are similar, suggesting that the correlated axes are the primary reason for the relation.

We also examined the relation between dust luminosity and the SFR, as shown in Fig. 13. We see that not only is the total dust luminosity but also the PDR and diffuse dust emission luminosities are well correlated with the SFR. As explained in Section 2.2, this is what is expected if a young stellar population is responsible for the dust heating and the total luminosity-weighted opacity of the sources, τ, does not vary arbitrarily among the sources.

8 DISCUSSION

In this section we discuss the properties of the detected compact sources of M83 in terms of gas masses and locations (Section 8.1), star formation (Section 8.2) and dust heating (Section 8.3).

8.1 Source gas masses and locations

The inferred dust masses of the compact sources lie within the range 10^4–10^6 $M_\odot$. These dust masses can be used to estimate the source gas masses as discussed in Section 6. We use a GDR of 100, which means the gas masses of the sources have values in the range 10^6–10^8 $M_\odot$. These values correspond to the high end of the molecular cloud mass distribution function derived both observationally (see e.g. Solomon et al. 1987; Rosolowsky 2005; Gratier et al. 2012) and by numerical simulations (e.g. Nimori et al. 2013). Furthermore, previous CO studies of nearby galaxies have highlighted the presence of very massive clouds with gas masses of the order of 10^7 $M_\odot$ or higher, which are usually referred to as giant molecular associations (GMAs; e.g. Vogel, Kulkarni & Scoville 1988; Koda et al. 2009; Muraoka et al. 2009). The high masses of our compact sources suggest that they are GMAs rather than less massive GMCs.

However, because dust continuum emission does not provide kinematical information, it is not possible to check whether the detected sources are gravitationally bound clouds. The smallest cloud radius we can measure is 130 pc due the 70 μm beam size

(6 arcsec). The majority of the detected sources are found on the spiral arms. Studies of the molecular gas in M83 have shown that most of the bright compact sources on the spiral arms are bound clouds in GMAs. Muraoka et al. (2009) examined CO in M83 and measured the virial parameter, α, defined as the ratio of the virial mass to the CO luminosity mass. They found that α is almost equal to unity in on-arm clouds, suggesting that they are in a gravitationally bound state (see also Rand, Lord & Higdon 1999; Lundgren et al. 2004). The resolution of their study was 7.5 arcsec, which is comparable to our resolution. Thus, it is quite likely that our sources are bound GMAs.

The spiral arms are the natural location where ISM gas is brought to higher densities, thus leading to the formation of massive clouds. Therefore, it is not surprising, given our resolution and sensitivity, that we only detect compact sources on the spiral structure. We note that the bar–spiral arm transition region harboured the most sources and that just few were detected along the length of the bar. Due to shear motions in bars, GMCs can be easily pulled apart (Downes et al. 1996). In contrast to spiral arms, bars exhibit lower SFRs and in some cases lower SFEs (Momose et al. 2010). Meanwhile, studies of atomic and molecular gas have shown that the most massive complexes are found in the bar–spiral arm transition region. This can be explained by orbit crowding when gas on highly elliptical orbits in the bar converges with the gas orbiting in the spiral structure (e.g. Kenney & Lord 1991). The location of the compact sources detected in the FIR is consistent with these findings in the gas.

8.2 SFRs and SFEs

One of the goals of this work has been to infer cloud gas masses using the dust emission of compact sources. Combined with a measure of the SFR, we can then examine the SFE in these regions.

There have been many recent studies that have examined star formation on spatially resolved scales. Typically, these studies have employed one of three methods: pixel-by-pixel analyses, where the SFR tracers and gas tracers are compared in individual pixels; azimuthal average analyses, where average values in radial bins are compared; or aperture photometry on compact sources bright in some SFR tracer such as Hα emission.

Our work differs in several key ways and, before discussing the results, we summarize these differences here. (1) We use the dust emission to detect the compact sources. While most studies have focused on aperture photometry of active star-forming regions (e.g. Calzetti et al. 2005; Kennicutt et al. 2007, etc.), a few have selected compact sources as seen in dust emission maps, which may be more akin to locating peaks in the gas (e.g. Schruba et al. 2010). However, there is a good correspondence between the detected FIR sources and star formation regions, which is demonstrated by the tight correlation between total infrared luminosities of the sources and their SFRs (see Fig. 13). (2) We perform a diffuse background subtraction of the dust emission using both a local background defined by GETSOURCES and one determined from nearby apertures in the interarm regions. Previous studies have performed a background subtraction on the star formation tracers but not on the gas mass (though see Rahman et al. 2011). (3) It is important to keep in mind, when comparing this work with others, that we analysed the total SFR and dust masses for individual sources while most studies consider the surface densities of the gas mass and SFR when examining trends between the two. The reason why we did not consider surface densities is that it is not clear what the source area should be, since the apparent size of the sources varies on each map depending on the map resolution. In addition, since most of the sources are not well resolved, it is not possible to determine the physical source area which is typically smaller than the PSF beam area.

As discussed in Section 2, previous works have found that, on relatively large spatial scales (>500 pc), clear correlations are found between the gas, SFR and dust as well as a tendency for these parameters to decline with radius. However, as we saw in Section 7, the compact regions detected in this study show a relatively constant SFR and dust mass with radius, albeit with large scatter and there is little to no correlation between the SFR and dust mass. Due to the small spatial scales of these sources (<300 pc), one does not expect to recover the relations found by averaging over much larger areas. Recently, it has become clear that on small spatial scales (<400 pc). the S-K relation between the gas surface density and SFR surface density breaks down (Schruba et al. 2010; Feldmann & Gnedin 2011; Calzetti, Liu & Koda 2012). This has been found to be even more prominent in the case where gas peaks are selected (Schruba et al. 2010). The scatter is due to the fact that individual GMCs and H II regions will show varying gas mass to SFRs depending on their evolutionary state. Averaging over large areas means that many objects in different states are averaged and the relation between SFR and gas mass is recovered.

The scales on which the SFR and gas mass surface density are measured play an important role in defining the relation (Liu et al. 2011). Typical SFR tracers suitable for relatively large galaxy regions are not straightforwardly applicable to small regions of sub-kpc scales. In fact, in this case, the intrinsic assumption that the stochastic characteristics of star formation are averaged out from the integration on large areas can easily break down (i.e. Calzetti et al. 2012). This happens because one ideally needs a complete sampling of the stellar IMF. Small regions may not encompass a large enough stellar population to do so. Furthermore, beyond the issue of sampling the stellar IMF, there is the problem of time averaging. The SFR is calibrated based on the assumption of a constant SFR over 100 Myr (Calzetti et al. 2007). While this is true for entire galaxies, on small scales this assumption may no longer hold and can create a large scatter in the relation.

Our sources have sizes of roughly 300 pc, and thus, we find a large scatter between the inferred gas mass and the SFR. We also note that our sources populate only a narrow range in FIR luminosity and dust mass (see Figs 5 and 6). Thus, we see a relatively constant SFR for sources with such similar characteristics. If we could populate the plot with lower mass regions, an S-K relation with considerable scatter might be recovered. Our results reflect stochasticity and the fact that individual star-forming regions can exhibit a range of SFRs for a given dust or gas mass. However, we should note a few other caveats that might introduce scatter into the relation.

First, it is possible that dust emission does a poor job of tracing molecular gas especially in light of our use of a constant GDR. There may be large variations in the GDR (i.e. due to metallicity variations), which means that our gas mass estimates might not be reliable. However, the compact regions all lie on the spiral arms and beyond the nuclear region of the galaxy. In F12, the largest variations in the GDR were seen in the central regions and, beyond, the GDR was quite constant. It is also possible that some of the peaks found in the dust emission are not associated with active star-forming regions. However, we found a correlation between the dust luminosity and the SFR, and studies like Verley et al. (2010) have found a tight correlation between compact regions in M33 and SFR tracers. We should also note that all of the sources were detected in the 70 μm map, which is also known as a good tracer of the SFR (Li et al. 2010).

A second possibility is that our background emission subtraction has introduced scatter. Rahman et al. (2011) showed that as one increases the amount of diffuse emission subtracted from the gas, the scatter in the S-K relation increases. However, particularly given that we are using dust emission, which may trace gas of different phases, it is important to account for a diffuse component.

Despite the large scatter, we find that the SFR varies little with the inferred gas mass and is roughly constant. This implies that the more massive clouds are less efficient at forming stars. A physical reason for this is that the more massive clumps might be more extended and thus have lower gas surface densities. Studies of GMCs have revealed that only the densest gas is directly associated with star formation. In this way, the more massive and thus extended regions may have roughly comparable SFRs (or lower SFEs). We note that we also found that there is a strong anticorrelation between the SFE and the inferred gas mass. However, as discussed in Section 7.3, this is largely a product of the correlated axis since mass appears both in the y- and x-axes [see Murray (2011), who examined galactic GMCs and found an anticorrelation which was attributed to a similar effect]. We also note that we find no radial variation of the SFE of the compact regions. Previous works, which have examined kpc-sized regions, have found that the SFE is relatively constant regardless of the variable considered (i.e. Leroy et al. 2008). This is consistent with our findings with radius.

8.3 Dust heating

We showed in Section 2.2 that the simultaneous presence of a correlation between the SFR and source dust luminosity as well as a correlation between the SFE and the dust temperature suggests that the radiation impinging on the dust mass is mainly produced by a local, young stellar population. Contrary to common lore, a strong correlation between the SFR and dust temperature should not be necessarily expected in this case. Indeed, we saw in Section 7 (see Figs 13 and 12) that while the dust temperature was only mildly correlated with the SFR, it was strongly correlated with the SFE. We also saw that the dust luminosity was correlated with the SFR (see Fig. 13). This supports a scenario where a young, local stellar population is powering the dust emission of the FIR bright sources of M83.

In Fig. 13, the solid line illustrates the maximum level of dust luminosity that can be powered by the young stellar population by assuming that all the luminosity from this population is absorbed and re-emitted by dust (optically thick case) using the following relation by Calzetti (2012):

$$\mathrm{SFR} = 2.8 \times 10^{-44} L_{\mathrm{dust}}. \quad (6)$$

This relation has been derived using the same assumptions on the star formation history, metallicity and IMF as the Hα-based calibration we used to infer SFR of the sources.

This line should delineate the maximum value, yet we find that many sources lie close to or above this limit. Specifically, we find that the percentage of sources that lie above or only within 2σ below this limit is 60 or 20 per cent in the HB or LB case, respectively. While it is surprising to find sources that lie above or close to this maximum limit, these findings can be explained in one of two ways.

First, it is possible that some regions are indeed very close to being completely optically thick and therefore the total dust luminosity will be approximately equal to the intrinsic young stellar population luminosity in those cases. However, this is unlikely because these regions are also Hα emitters, which means, by definition, that at least some fraction of the young stellar population luminosity is able to escape unabsorbed (at least through re-emission in Hα). Furthermore, we checked that the differences between the observed dust luminosities and the dust luminosities for an optically thick case, predicted by the relation in equation (6), do not depend on the ratio F(Hα)/SFR[Hα $-$ 24 μm]. This suggests that the scatter of the observed points is not driven by differences in attenuation.

Secondly, it is possible that there is a local older stellar population or stellar populations outside the projected source area contributing substantially to the heating. In this case, the approximate equality between dust and young stellar population luminosity would be reached through this extra heating from other radiation sources. Thus, the infrared total luminosity could still be used as an SFR indicator in those cases despite the fact that the dust heating is not powered exclusively by a local, young stellar population (see Bendo et al. 2012 also). This might explain why the recent work of Verley et al. (2010) and Boquien et al. (2010) showed that the single *Herschel* 100, 160 and 250 μm band luminosities of individual sources in M33 are good tracers of SFR, since most of the dust luminosity is emitted at FIR wavelengths.

We should note that the SFE versus T_{dust} correlation is at least partially driven by the M_{dust} versus T_{dust} anticorrelation (more evident for the LB measurement), since the SFR alone does not correlate with M_{dust} and only mildly with T_{dust}. There are multiple potential explanations for an anticorrelation between mass and temperature. One possible explanation is that it is due to the different evolutionary stages of the sources, with the more massive sources having a relatively lower number of young, recently formed stars. In this way, the radiation field would be less intense for massive sources and the dust would be cooler. Alternatively, it could be that the more massive sources are more efficient at shielding radiation originating from outside the local region. As outlined in the previous paragraph, there is likely some heating due to other stellar populations other than just the local, young population, and thus such shielding could keep more massive sources cooler.

The anticorrelation between dust temperature and mass could be in part due to the lower limit in dust luminosity for the sources. Fig. 14 shows the inferred dust masses versus dust temperatures with the plotted points colour-coded depending on the source total dust luminosity. Since most of the dust luminosity is emitted at FIR wavelengths where $L_{\mathrm{dust}} \propto M_{\mathrm{dust}} T_{\mathrm{dust}}^{4+\beta}$, the points correspond to higher total dust luminosities while moving from the bottom-left to the upper-right region of the plot. From this figure, one can see that there is a lower limit in luminosity ($\approx$5–6 $\times$ 10^{40} erg s^{-1}), determined by the minimum fluxes for source detection. This explains why there are no sources populating the lower-left part of the

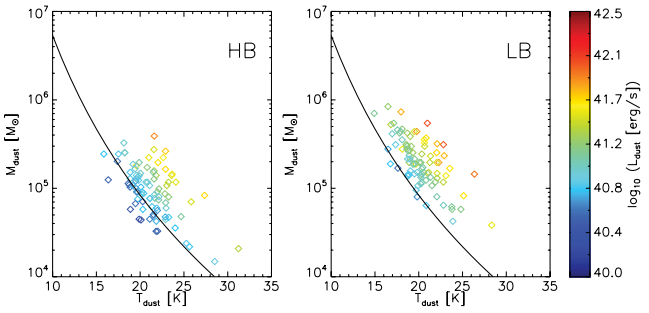

Figure 14. Source dust masses versus dust temperature for the HB (left) and LB (right) measurements. The points are colour-coded based on their total dust luminosity. The solid line represents the relation $L_{\mathrm{dust}} \propto M_{\mathrm{dust}}\ T_{\mathrm{dust}}^{6}$ for $L_{\mathrm{dust}} = 6 \times 10^{40}$erg s^{-1}.

diagram. The steepness of the observed anticorrelation is consistent with the $4 + \beta$ exponent (with $\beta = 2$), as shown by the line in Fig. 14. However, higher mass sources do not populate uniformly the entire range of temperatures in the upper-right part of the diagram, where source detection would easily be possible. Therefore, while the low-luminosity limit may contribute to the anticorrelation between dust temperature and mass, it cannot fully account for it. Thus, there should be at least some physical restrictions at play.

We note that the lower limit to the luminosity range explored in our analysis does introduce a bias that should be taken into account. Essentially, our sources are the brightest FIR compact sources in the disc of M83 and they are associated with the high end of the molecular cloud mass distribution. As discussed in Section 8.1, the sources are associated with gas masses in the range $\approx 10^6$–10^8 $M_\odot$, while their total dust luminosities are in the range ≈ 0.5–5×10^{41} erg s^{-1}. The results of this work should be considered valid only within these parameter ranges.

We found a mild correlation between SFR and $T_{\rm dust}$. However, as shown in Appendix C, a better correlation is found when plotting the inferred 70/160 μm flux ratio versus the SFR. The difference between the two cases is due to the fact that $T_{\rm dust}$ in our SED fitting procedure refers to the cold dust temperature of the diffuse dust component. Meanwhile, the observed 70 and 160 μm fluxes have contributions from both the diffuse component and the PDR component. Nonetheless, in Appendix C we also show that the correlation between SFE and 70/160 μm flux ratio is clearly tighter and this is consistent with the arguments presented in Section 2.2 and very similar to the strong correlation found by plotting SFE versus $T_{\rm dust}$.

Pixel-by-pixel analyses have tended to find varying results with no strong consensus for a correlation between SFR and modified blackbody dust temperatures or colour temperatures. We should note that the pixel-by-pixel analyses have considered the star formation rate surface density (hereafter SFRSD) as opposed to the SFR used here. For M83, F12 found a correlation between the SFRSD and $T_{\rm dust}$. A similar result for M83 has been found by Bendo et al. (2012) when comparing the 70/160 μm flux ratio with the observed Hα brightness, uncorrected for internal dust attenuation. However, Bendo et al. (2012) found a weaker correlation for M81 and NGC 2403.[7] Boquien et al. (2011) found a mild correlation between SFRSD and the 70/160 μm flux ratio for M33. In addition, Smith et al. (2012) for the Andromeda galaxy and Skibba et al. (2012) for the Large and Small Magellanic Clouds found no or only a weak correlation between SFRSD and $T_{\rm dust}$. Therefore, it seems that in general the correlation between SFR versus tracers of dust temperature is not observed to be very strong when one considers either total SFRs for individual FIR sources or SFR averages on areas equivalent to pixel sizes. As explained in Section 2.2, this is expected even for the case where young stellar populations are responsible for the dust heating because the dust temperature also depends on the dust mass and the total luminosity-weighted optical depth (see equation 4), which are not uniform throughout a galaxy disc.

As we have seen, while isolating FIR bright sources has highlighted the presence of interesting correlations between the inferred source parameters, the narrow range of luminosities of the sources has introduced a potentially important bias. In order to elucidate the influence of this bias on the inferred relationships, we need to expand this work to include sources within a wider range of luminosities, particularly fainter sources. To do so, we plan a follow-up study which will include other spiral galaxies that are even closer (i.e. NGC 2403 and M33). The closer proximity will allow for an even better spatial resolution, which is necessary to detect sources in a wider range of luminosities and determine if the results for the GMAs in M83 are also valid for GMCs in other galaxies.

[7] The weaker correlation is attributed to the dust heating by bulge stars in M81 and artefacts in the images of NGC 2403; see the discussion in that paper.

9 CONCLUSIONS

The main aim of this paper has been the investigation of the star formation and dust heating properties of the compact FIR bright sources as observed on the *Herschel* maps of the nearby spiral galaxy M83. By combining the source detection and photometry algorithm GETSOURCES, the dust emission SED fitting method of NA10 and the [Hα − 24 μm] SFR calibration by Calzetti et al. (2007), we have developed a new procedure to determine gas masses, radiation field intensities, cold dust temperatures, dust luminosities, SFRs and SFEs associated with those sources.

The main results of our analysis are the following.

(i) We have found that the well-detected compact FIR sources are mostly associated with GMAs, with gas masses in the range 10^6–10^8 $M_\odot$ and dust total infrared luminosities in the range 0.5×10^{41}–10^{42} erg s^{-1}. The majority of the sources are located on the spiral arms of M83 with only a few sources found in the interarm and within the bar in the central region of M83.

(ii) None of the inferred physical quantities for the sources shows a strong variation with radius, including SFRs, gas masses and dust temperatures. Previous studies have usually found radial variation for these quantities, although only after averaging on larger areas including interarm regions and without subtracting any local background.

(iii) The SFR does not seem to correlate strongly with the gas mass of the sources. The lack of correlation is most likely due to the small spatial scales considered (≈200–300 pc) and/or the relatively small range of inferred gas masses.

(iv) The SFE, defined as SFR/$M_{\rm gas}$, shows an anticorrelation with source gas mass. This finding suggests that the more massive GMAs are less efficient in forming stars in the last few Myr. However, we note that this anticorrelation is a consequence of the roughly constant SFR with inferred gas mass.

(v) We found that the SFR correlates well with total dust luminosity, which is consistent with a scenario where dust is predominantly heated by the local young stellar population. However, 20–60 per cent of the sources show dust luminosities which are greater than or only 2σ below those predicted when the heating is due only to a local young stellar population, embedded in an optically thick dust distribution. It is unlikely that the sources are completely optically thick, as they are also bright in Hα. Thus, it seems that there must be some extra heating by either a local older stellar population or by an external radiation field.

(vi) We found a correlation between the SFE and $T_{\rm dust}$ which is tighter than the mild correlation we found between SFR and $T_{\rm dust}$. This is expected if the dust is heated primarily by recent star formation.

(vii) We found a mild anticorrelation between dust and mass temperature. While our sources have a low-luminosity limit, which may contribute to this anticorrelation, we find that this cannot fully account for it. Thus, we speculate that the more massive sources are more efficient at shielding from an impinging radiation field or that more massive sources are in an earlier stage of star formation.

We plan to use the same procedure presented in this pilot work on a set of nearby galaxies observed by *Herschel*. This will help to further clarify the origin of the observed correlations and their implications for star formation and dust heating associated with FIR bright sources on galactic scales.

ACKNOWLEDGEMENTS

We are grateful to the anonymous referee for his/her careful reading of this paper and his/her comments. KF acknowledges helpful conversations with S. J. Kiss, V. Könyves, P. G. Martin, A. Men'shchikov, M. Reid and R. Skibba. This research was supported by grants from the Canadian Space Agency and the Natural Science and Engineering Research Council of Canada (PI: C. D. Wilson). MPS has been funded by the Agenzia Spaziale Italiana (ASI) under contract I/005/11/0. PACS has been developed by a consortium of institutes led by MPE (Germany) and including UVIE (Austria); KU Leuven, CSL, IMEC (Belgium); CEA, LAM (France); MPIA (Germany); INAF-IFSI/OAA/OAP/OAT, LENS, SISSA (Italy); IAC (Spain). This development has been supported by the funding agencies BMVIT (Austria), ESA-PRODEX (Belgium), CEA/CNES (France), DLR (Germany), ASI/INAF (Italy) and CICYT/MCYT (Spain). SPIRE has been developed by a consortium of institutes led by Cardiff University (UK) and including Univ. Lethbridge (Canada); NAOC (China); CEA, LAM (France); IFSI, Univ. Padua (Italy); IAC (Spain); Stockholm Observatory (Sweden); Imperial College London, RAL, UCL-MSSL, UKATC, Univ. Sussex (UK); and Caltech, JPL, NHSC, Univ. Colorado (USA). This development has been supported by national funding agencies: CSA (Canada); NAOC (China); CEA, CNES, CNRS (France); ASI (Italy); MCINN (Spain); SNSB (Sweden); STFC (UK); and NASA (USA). HIPE is a joint development by the Herschel Science Ground Segment Consortium, consisting of ESA, the NASA Herschel Science Center, and the HIFI, PACS and SPIRE consortia. This research has made use of the NASA/IPAC Extragalactic Database (NED) which is operated by the Jet Propulsion Laboratory, California Institute of Technology, under contract with the National Aeronautics and Space Administration.

REFERENCES

Aniano G., Draine B. T., Gordon K. D., Sandstrom K., 2011, PASP, 123, 1218
Aniano G. et al., 2012, ApJ, 756, 138
Auld R. et al., 2013, MNRAS, 428, 1880
Bendo G. J. et al., 2010, A&A, 518, L65
Bendo G. J. et al., 2012, MNRAS, 419, 1833
Bernstein R. A., Freedman W. L., Madore B. F., 2002, ApJ, 571, 107
Bertin E., Arnouts S., 1996, A&AS, 117, 393
Bigiel F., Leroy A., Walter F., Brinks E., de Blok W. J. G., Madore B., Thornley M. D., 2008, AJ, 136, 2846
Bigiel F. et al., 2011, ApJ, 730, L13
Blanc G. A., Heiderman A., Gebhardt K., Evans N. J., II, Adams J., 2009, ApJ, 704, 842
Bolatto A. D., Wolfire M., Leroy A. K., 2013, preprint (arXiv:1301.3498)
Boquien M. et al., 2010, A&A, 518, L70
Boquien M. et al., 2011, AJ, 142, 111
Boquien M. et al., 2012, A&A, 539, A145
Boselli A., Lequeux J., Gavazzi G., 2002, Ap&SS, 281, 127
Boselli A., Boissier S., Cortese L., Buat V., Hughes T. M., Gavazzi G., 2009, ApJ, 706, 1527
Calzetti D., 2012, preprint (arXiv:1208.2997)
Calzetti D. et al., 2005, ApJ, 633, 871
Calzetti D. et al., 2007, ApJ, 666, 870
Calzetti D., Liu G., Koda J., 2012, ApJ, 752, 98
Corbelli E. et al., 2012, A&A, 542, A32
Crosthwaite L. P., Turner J. L., Buchholz L., Ho P. T. P., Martin R. N., 2002, AJ, 123, 1892
Dale D. A. et al., 2009, ApJ, 703, 517
Dale D. A. et al., 2012, ApJ, 745, 95
Davies J. I. et al., 2012, MNRAS, 419, 3505
Downes D., Reynaud D., Solomon P. M., Radford S. J. E., 1996, ApJ, 461, 186
Draine B. T., 2003, ARA&A, 41, 241
Draine B. T., Li A., 2007, ApJ, 657, 810
Eales S. A. et al., 2010, A&A, 518, L62
Eales S. et al., 2012, ApJ, 761, 168
Engelbracht C. W. et al., 2010, A&A, 518, L56
Feldmann R., Gnedin N. Y., 2011, ApJ, 727, L12
Ferguson A. M. N., Wyse R. F. G., Gallagher J. S., III, Hunter D. A., 1996, AJ, 111, 2265
Fischera J., Dopita M. A., 2008, ApJS, 176, 164
Foyle K., Rix H.-W., Walter F., Leroy A. K., 2010, ApJ, 725, 534
Foyle K. et al., 2012, MNRAS, 421, 2917 (F12)
Gratier P. et al., 2012, A&A, 542, A108
Griffin M. J. et al., 2010, A&A, 518, L3
Groves B., Dopita M. A., Sutherland R. S., Kewley L. J., Fischera J., Leitherer C., Brandl B., van Breugel W., 2008, ApJS, 176, 438
Groves B. et al., 2012, MNRAS, 426, 892
Guhathakurta P., Draine B. T., 1989, ApJ, 345, 230
Helou G. et al., 2004, ApJS, 154, 253
Hildebrand R. H., 1983, QJRAS, 24, 267
Hirota A. et al., 2011, ApJ, 737, 40
Kenney J. D. P., Lord S. D., 1991, ApJ, 381, 118
Kennicutt R. C., Jr, 1989, ApJ, 344, 685
Kennicutt R. C., Jr, 1998, ApJ, 498, 541
Kennicutt R. C., Evans N. J., 2012, ARA&A, 50, 531
Kennicutt R. C., Jr et al., 2007, ApJ, 671, 333
Koda J. et al., 2009, ApJ, 700, 132
Law K.-H., Gordon K. D., Misselt K. A., 2011, ApJ, 738, 124
Lee J. C. et al., 2009, ApJ, 706, 599
Leroy A. K., Walter F., Brinks E., Bigiel F., de Blok W. J. G., Madore B., Thornley M. D., 2008, AJ, 136, 2782
Leroy A. K. et al., 2012, AJ, 144, 3
Li Y., Calzetti D., Kennicutt R. C., Hong S., Engelbracht C. W., Dale D. A., Moustakas J., 2010, ApJ, 725, 677
Liu G., Koda J., Calzetti D., Fukuhara M., Momose R., 2011, ApJ, 735, 63
Lundgren A. A., Wiklind T., Olofsson H., Rydbeck G., 2004, A&A, 413, 505
Markwardt C. B., 2009, in Bohlender D. A., Durand D., Dowler P., eds, ASP Conf. Ser. Vol. 411, Astronomical Data Analysis Software and Systems XVIII. Astron. Soc. Pac., San Francisco, p. 251
Mathis J. S., Mezger P. G., Panagia N., 1983, A&A, 128, 212
Men'shchikov A., André Ph., Didelon P., Motte F., Hennemann M., Schneider N., 2012, A&A, 542, 81
Meurer G. R. et al., 2006, ApJS, 165, 307
Momose R., Okumura S. K., Koda J., Sawada T., 2010, ApJ, 721, 383
Muñoz-Mateos J. C. et al., 2009, ApJ, 701, 1965
Muraoka K. et al., 2009, ApJ, 706, 1213
Murray N., 2011, ApJ, 729, 133
Natale G. et al., 2010, ApJ, 725, 955 (NA10)
Nimori M., Habe A., Sorai K., Watanabe Y., Hirota A., Namekata D., 2013, MNRAS, 429, 2175
Pilbratt G. L. et al., 2010, A&A, 518, 1
Poglitsch A. et al., 2010, A&A, 518, L2
Pohlen M. et al., 2010, A&A, 518, L72
Popescu C. C., Tuffs R. J., 2002, MNRAS, 335, L41
Popescu C. C., Tuffs R. J., Dopita M. A., Fischera J., Kylafis N. D., Madore B. F., 2011, A&A, 527, 109
Rahman N. et al., 2011, ApJ, 730, 72
Rand R. J., Lord S. D., Higdon J. L., 1999, ApJ, 513, 720

Relaño M., Kennicutt R. C., Jr, Eldridge J. J., Lee J. C., Verley S., 2012, MNRAS, 423, 2933
Rosolowsky E., 2005, PASP, 117, 1403
Roussel H., 2012, preprint (arXiv:1205.2576)
Sandstrom K. M. et al., 2012, preprint (arXiv:1212.1208)
Schlegel D. J., Finkbeiner D. P., Davis M., 1998, ApJ, 500, 525
Schmidt M., 1959, ApJ, 129, 243
Schruba A., Leroy A. K., Walter F., Sandstrom K., Rosolowsky E., 2010, ApJ, 722, 1699
Shetty R., Glover S. C., Dullemond C. P., Klessen R. S., 2011, MNRAS, 412, 1686
Skibba R. A. et al., 2012, ApJ, 761, 42
Smith M. W. L. et al., 2012, ApJ, 756, 40
Solomon P. M., Rivolo A. R., Barrett J., Yahil A., 1987, ApJ, 319, 730
Stutzki J., Guesten R., 1990, ApJ, 356, 513
Thim F., Tammann G. A., Saha A., Dolphin A., Sandage A., Tolstoy E., Labhardt L., 2003, ApJ, 590, 256
Tilanus R. P. J., Allen R. J., 1993, A&A, 274, 707
Verley S. et al., 2010, A&A, 518, 68
Vogel S. N., Kulkarni S. R., Scoville N. Z., 1988, Nat, 334, 402
Voit G. M., 1991, ApJ, 379, 122
Walter F., Brinks E., de Blok W. J. G., Bigiel F., Kennicutt R. C., Jr., Thornley M. D., Leroy A., 2008, AJ, 136, 2563
Williams J. P., de Geus E. J., Blitz L., 1994, ApJ, 428, 693
Wong T., Blitz L., 2002, ApJ, 569, 157
Zhu Y.-N., Wu H., Cao C., Li H.-N., 2008, ApJ, 686, 155

APPENDIX A: RESOLUTION TESTS

We test for any systematic errors in the process of detecting and measuring fluxes of the compact sources using GETSOURCES. To do so, we take the 70 μm map with 6 arcsec resolution and degrade its resolution to match that of the 160 μm map (12 arcsec), the 250 μm map (18.2 arcsec) and the 350 μm (24.5 arcsec) using the convolution kernels of Aniano et al. (2011). We then rerun the extraction process using these series of maps. We can then compare how the flux of the sources is affected by the degradation of the resolution. In principle, at each resolution, the flux should be the same for each source. However, particularly in crowded regions, the source flux is more complicated to determine as the resolution is degraded. Fig. A1 compares how the source flux at the degraded resolution compares to the original. In general, we find that the flux is somewhat overestimated as the resolution is degraded. Half of the sources fall within the uncertainties on the measurements and the majority lie within a factor of 2 of the flux determined at the 6 arcsec resolution. We also tested how such a systematic uncertainty could affect the results of the inferred dust temperature and mass. By applying the average correction factors to the source

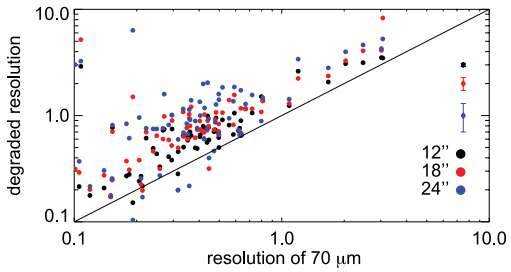

Figure A1. Total flux of the sources measured by GETSOURCES using the degraded 70 μm maps versus the total flux of those sources measured in the 70 μm map in its native resolution. The median uncertainties for each resolution are shown on the right. At poorer resolutions, the source flux is increasingly overestimated.

FIR flux measurements (see Section 4.2) and performing SED fitting as described in Section 5, we found an average relative difference in dust mass of ≈50 per cent and an average difference of 2 K for the dust temperatures. Although non-negligible, the possible systematic effect highlighted by this test is not large enough to affect the main conclusions of this work.

APPENDIX B: COMPARISON WITH MODIFIED BLACKBODY FITS

We compare the results of our two-component SED fitting method, by determining the dust temperature and mass using a modified blackbody fit to the FIR emission (70–350 μm).

We use a modified blackbody of the form

$$S_\lambda = N B_\lambda(T)\lambda^{-\beta}, \tag{B1}$$

where S_λ is the flux density, $B_\lambda(T)$ is the Planck function, N is a constant related to the column density of the material and β is the dust emissivity index. We hold β at a constant value of 2, based on the average value found by F12. We fit the points using MPFIT, a least-squares curve fitting routine for IDL (Markwardt 2009). We refer to the temperature and dust masses determined by this technique as $T_{\rm dust,\,MB}$ and $M_{\rm dust,\,MB}$, respectively.

Figs B1 and B2 compare the temperatures and masses derived from the SED fitting with those from a modified blackbody fit. There is close agreement with the temperatures, although the modified blackbody dust temperatures tend to be slightly higher. The masses found by the SED fitting are larger than those from the modified blackbody fits with a median ratio of a factor of 1.4. Dust emission models typically have higher masses than modified blackbody fits, because the latter do not encompass the full range of temperatures of the dust as they use only the FIR maps (Dale et al. 2012). In F12, they found that fitting the SED using the dust emission models of

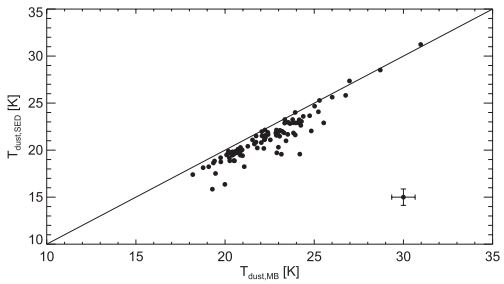

Figure B1. Comparison of the dust temperature derived by the SED fitting to that obtained by a modified blackbody fit of the FIR wavelengths. The median uncertainties are shown on the bottom right.

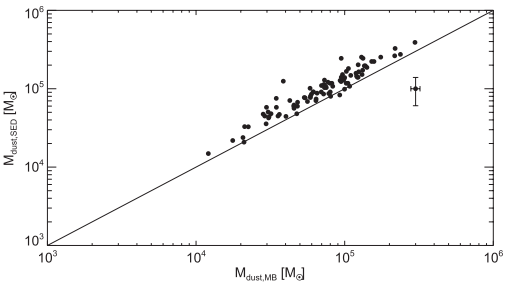

Figure B2. Comparison of the dust mass derived by the SED fitting to that obtained by a modified blackbody fit of the FIR wavelengths.

Draine & Li (2007) the total mass of M83 was greater by a factor of 1.3 than those found using a modified blackbody fit.

APPENDIX C: COLOUR CORRELATIONS

Many previous works that have examined dust heating mechanisms and correlations with recent SFR tracers have used dust emission colours as opposed to SED fitting parameters (i.e. Boquien et al. 2011; Bendo et al. 2012). For the purposes of comparison, we also examine how the dust emission colours vary with radius and with the star formation parameters, SFR and SFE.

We consider the colour ratios of 70 to 160 μm, 160 to 250 μm and 250 to 350 μm emission. In following what we have done in the previous sections, we consider both measures of the compact sources.

Fig. C1 shows how the colours vary with radius. As we saw with the SED fitting parameters, for both measures of the compact sources, we find no or just a weak trend in the colours with radius. Both Bendo et al. (2012) and Boquien et al. (2011) found in their pixel-by-pixel analyses that the FIR colours present decreasing radial trends. Our measurements show that, when compact regions are separated, they do not seem to behave in the same way.

Fig. C2 shows how the colours correlate with the SFR. Bendo et al. (2012) and Boquien et al. (2011) highlighted the presence of correlations between SFR and FIR colours, especially the 70-to-160 μm intensity ratio. This finding was used to imply that at shorter FIR wavelengths, the dust heating is powered mostly by recent star formation. We find a mild correlation between the SFR and 70-to-160 μm intensity ratio. This correlation is stronger than that seen between the SFR and the dust temperature $T_{\rm dust}$ inferred by SED fitting. The difference in the results when using the 70-to-160 μm intensity ratio and $T_{\rm dust}$ is due to the fact that the latter is the dust temperature associated with the cold diffuse dust component

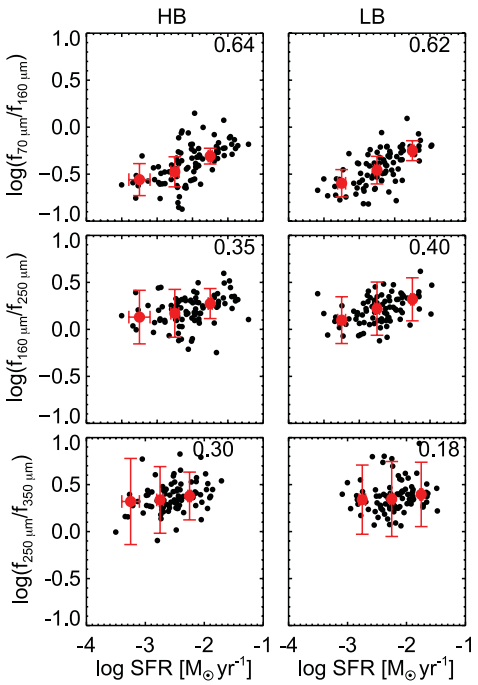

Figure C2. Ratio of 70 to 160 μm emission (top), 160 to 250 μm emission (second from top) and 250 to 350 μm emission (bottom) for the compact sources with HB subtraction (left) and LB subtraction (right) versus the SFR measured in each case.

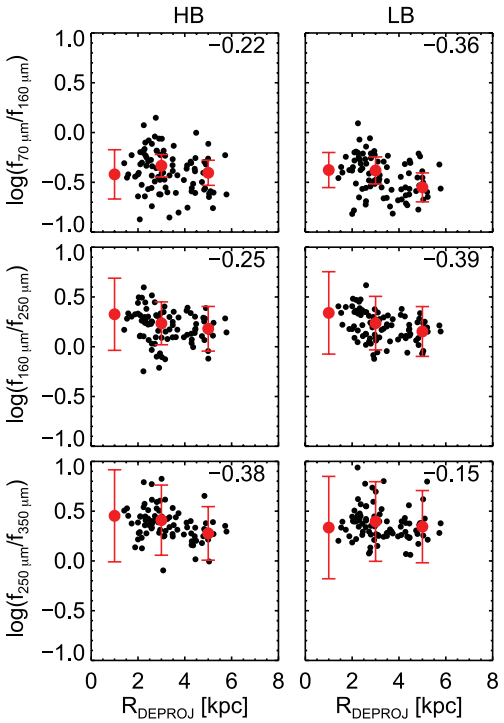

Figure C1. Ratio of 70 to 160 μm emission (top), 160 to 250 μm emission (second from top) and 250 to 350 μm emission (bottom) for the compact source measurements with HB subtraction (left) and LB subtraction (right) versus deprojected radial position.

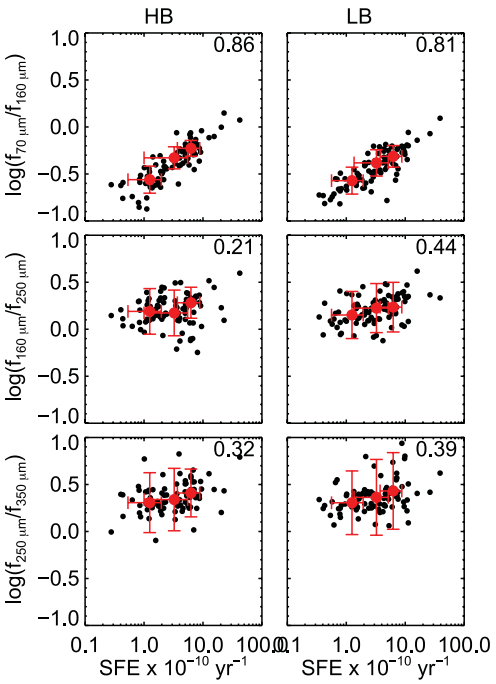

Figure C3. Ratio of 70 to 160 μm emission (top), 160 to 250 μm emission (second from top) and 250 to 350 μm emission (bottom) for the compact source measurements from GETSOURCES (left) and alternative compact source measurements (right) versus the SFE measured in each case.

in the SED fitting. At both 70 and 160 μm, a part of the emission is contributed by the PDR component as well; thus, the FIR colours fitted by the diffuse dust component are usually slightly different from the observed ones.

However, we note that there is a strong correlation between the SFE and the 70-to-160 μm intensity ratio (see Fig. C3), which is very similar with what we saw in Section 7.3 for the correlation observed between SFE and $T_{\rm dust}$. On the other hand, we did not find any strong correlation of the 160/250 μm or 250/350 μm flux ratio with SFR or SFE. This might indicate that the dust emission at these wavelengths is more affected by heating from older stellar populations. However, one should also note that the flux uncertainties are quite large at longer wavelengths and, as a consequence, there could also be a stronger scatter hiding the presence of intrinsic correlations.

APPENDIX D: SOURCE FLUXES

Table D1. HB measurement source fluxes and positions.

	RA (°)	δ (°)	$F_{8\,\mu m}$ (mJy)	$F_{24\,\mu m}$ (mJy)	$F_{70\,\mu m}$ (mJy)	$F_{160\,\mu m}$ (mJy)	$F_{250\,\mu m}$ (mJy)	$F_{350\,\mu m}$ (mJy)	F(Hα) (μJy)
1	204.278 67	−29.826 725	79 ± 6	190 ± 10	2710 ± 150	3690 ± 410	1640 ± 410	720 ± 220	51 ± 2
2	204.264 33	−29.900 421	35 ± 5	139 ± 9	1495 ± 92	2490 ± 290	1320 ± 310	650 ± 210	36 ± 2
3	204.221 28	−29.858 999	89 ± 8	180 ± 10	2410 ± 160	3790 ± 680	1830 ± 480	650 ± 220	82 ± 3
4	204.282 71	−29.854 724	68 ± 7	107 ± 7	2090 ± 130	3060 ± 500	1540 ± 450	410 ± 200	34 ± 3
5	204.231 87	−29.830 846	88 ± 7	73 ± 6	1860 ± 120	3120 ± 370	1440 ± 410	580 ± 210	84 ± 3
6	204.226 52	−29.884 745	70 ± 6	100 ± 10	2010 ± 140	2530 ± 600	910 ± 360	330 ± 180	98 ± 3
7	204.228 94	−29.885 796	48 ± 6	80 ± 9	1840 ± 140	1550 ± 560	390 ± 310	–	80 ± 3
8	204.221 72	−29.882 527	36 ± 5	81 ± 8	1580 ± 120	1900 ± 500	1620 ± 430	710 ± 220	40 ± 3
9	204.219 30	−29.863 860	120 ± 10	140 ± 10	2840 ± 200	5690 ± 960	1830 ± 490	1370 ± 290	30 ± 4
10	204.220 46	−29.880 233	102 ± 8	140 ± 10	1630 ± 120	3160 ± 610	1890 ± 460	590 ± 210	79 ± 3
11	204.219 71	−29.852 660	53 ± 6	62 ± 9	1180 ± 110	2110 ± 340	1230 ± 420	460 ± 200	65 ± 4
12	204.269 57	−29.849 437	87 ± 8	106 ± 9	2260 ± 160	3820 ± 730	1900 ± 470	800 ± 230	127 ± 3
13	204.284 87	−29.869 891	84 ± 8	71 ± 6	1427 ± 98	2430 ± 380	1280 ± 400	500 ± 210	63 ± 3
14	204.228 00	−29.882 334	62 ± 6	58 ± 8	1620 ± 120	3370 ± 710	2610 ± 530	940 ± 240	16 ± 2
15	204.286 34	−29.858 535	31 ± 5	49 ± 6	531 ± 60	1970 ± 370	980 ± 390	370 ± 200	8 ± 3
16	204.280 83	−29.852 275	150 ± 10	270 ± 20	3850 ± 250	5850 ± 840	4590 ± 850	1330 ± 300	104 ± 4
17	204.168 14	−29.855 863	29 ± 2	30 ± 2	554 ± 31	940 ± 160	490 ± 160	216 ± 74	40.2 ± 0.9
18	204.225 54	−29.844 806	20 ± 4	60 ± 5	710 ± 67	1530 ± 290	640 ± 370	340 ± 190	70 ± 3
19	204.214 63	−29.883 342	25 ± 5	37 ± 7	666 ± 89	770 ± 280	1250 ± 350	390 ± 190	15 ± 3
20	204.283 97	−29.881 946	37 ± 6	38 ± 4	820 ± 74	1790 ± 280	1010 ± 320	430 ± 200	42 ± 3
21	204.208 49	−29.878 634	33 ± 4	42 ± 5	814 ± 92	2420 ± 330	960 ± 300	530 ± 210	20 ± 4
22	204.269 97	−29.823 576	50 ± 6	44 ± 6	986 ± 91	1830 ± 320	1030 ± 350	300 ± 180	86 ± 3
23	204.291 86	−29.858 028	19 ± 4	12 ± 4	383 ± 58	580 ± 260	730 ± 340	220 ± 180	43 ± 4
24	204.252 44	−29.905 010	46 ± 6	23 ± 3	451 ± 50	1610 ± 230	1130 ± 290	570 ± 190	38 ± 2
25	204.212 23	−29.844 608	106 ± 8	99 ± 8	2040 ± 140	3110 ± 410	1390 ± 410	790 ± 230	108 ± 3
26	204.218 77	−29.863 393	16 ± 4	39 ± 8	478 ± 84	760 ± 560	1350 ± 420	–	83 ± 3
27	204.288 31	−29.849 784	23 ± 4	25 ± 4	633 ± 65	450 ± 260	360 ± 310	–	36 ± 4
28	204.246 29	−29.907 226	34 ± 3	18 ± 2	453 ± 50	1220 ± 210	820 ± 250	380 ± 170	45 ± 2
29	204.188 35	−29.879 014	16 ± 2	20 ± 2	350 ± 33	810 ± 200	590 ± 210	330 ± 110	16 ± 3
30	204.180 91	−29.872 982	12 ± 2	25 ± 3	317 ± 39	630 ± 180	540 ± 200	119 ± 76	46 ± 4
31	204.231 24	−29.845 585	69 ± 7	55 ± 5	730 ± 64	1860 ± 430	590 ± 370	310 ± 180	18 ± 2
32	204.291 58	−29.819 528	16 ± 4	17 ± 2	447 ± 61	450 ± 250	270 ± 140	170 ± 110	61 ± 4
33	204.223 54	−29.813 422	13 ± 2	15 ± 2	300 ± 26	540 ± 160	360 ± 180	340 ± 140	44 ± 2
34	204.297 32	−29.831 076	14 ± 4	16 ± 2	360 ± 47	770 ± 280	580 ± 230	270 ± 150	39 ± 3
35	204.277 95	−29.823 031	12 ± 3	21 ± 5	241 ± 44	1530 ± 300	780 ± 290	260 ± 170	15 ± 2
36	204.248 19	−29.810 471	59 ± 5	47 ± 3	908 ± 57	1780 ± 240	820 ± 260	330 ± 150	68 ± 2
37	204.267 38	−29.899 060	13 ± 4	17 ± 4	381 ± 46	1590 ± 250	790 ± 270	410 ± 190	28 ± 2
38	204.236 65	−29.880 081	46 ± 7	52 ± 6	1040 ± 110	2730 ± 810	1260 ± 380	440 ± 190	15 ± 2
39	204.211 63	−29.866 269	23 ± 5	21 ± 5	423 ± 83	460 ± 250	430 ± 260	150 ± 150	20 ± 4
40	204.311 40	−29.843 049	22 ± 3	14 ± 2	329 ± 33	810 ± 250	400 ± 160	250 ± 120	– -
41	204.258 32	−29.925 232	25 ± 3	16 ± 2	313 ± 25	790 ± 170	410 ± 150	230 ± 100	47 ± 2
42	204.282 58	−29.887 080	11 ± 4	19 ± 4	314 ± 52	720 ± 220	340 ± 240	–	22 ± 3
43	204.212 62	−29.876 963	34 ± 4	32 ± 5	884 ± 92	1350 ± 310	660 ± 310	170 ± 160	23 ± 3
44	204.279 39	−29.857 758	10 ± 4	20 ± 4	312 ± 60	1360 ± 540	630 ± 320	390 ± 200	25 ± 3
45	204.288 41	−29.857 795	170 ± 10	120 ± 10	3080 ± 210	4000 ± 650	1220 ± 470	300 ± 200	72 ± 6
46	204.272 39	−29.821 631	17 ± 4	17 ± 5	424 ± 62	1140 ± 270	770 ± 290	370 ± 180	32 ± 2
47	204.231 90	−29.881 713	27 ± 5	12 ± 5	724 ± 84	2010 ± 680	950 ± 350	690 ± 220	21 ± 2
48	204.175 84	−29.875 390	37 ± 4	12 ± 2	266 ± 38	1530 ± 230	1180 ± 270	480 ± 110	8 ± 4

Table D1 – *continued*

	RA (°)	δ (°)	$F_{8\,\mu m}$ (mJy)	$F_{24\,\mu m}$ (mJy)	$F_{70\,\mu m}$ (mJy)	$F_{160\,\mu m}$ (mJy)	$F_{250\,\mu m}$ (mJy)	$F_{350\,\mu m}$ (mJy)	$F(H\alpha)$ (μJy)
49	204.260 47	−29.832 599	25 ± 3	20 ± 2	374 ± 42	1350 ± 280	750 ± 380	350 ± 190	10 ± 2
50	204.263 16	−29.827 777	92 ± 9	37 ± 4	674 ± 82	1740 ± 370	1410 ± 490	210 ± 170	34 ± 2
51	204.267 79	−29.925 076	28 ± 3	19 ± 2	428 ± 34	1550 ± 190	810 ± 190	400 ± 120	38 ± 3
52	204.280 75	−29.909 675	47 ± 4	37 ± 3	605 ± 44	1400 ± 220	610 ± 180	250 ± 140	77 ± 3
53	204.320 62	−29.886 212	14 ± 2	12 ± 1	223 ± 19	410 ± 110	450 ± 170	270 ± 110	23.5 ± 0.8
54	204.234 95	−29.885 641	15 ± 5	18 ± 6	294 ± 64	780 ± 580	280 ± 260	–	–
55	204.285 09	−29.878 952	26 ± 5	17 ± 4	539 ± 63	1010 ± 250	600 ± 310	240 ± 190	22 ± 4
56	204.271 36	−29.804 832	41 ± 3	27 ± 2	695 ± 43	1450 ± 290	590 ± 180	250 ± 110	39 ± 2
57	204.244 38	−29.801 254	8 ± 2	10 ± 2	213 ± 31	280 ± 140	360 ± 150	200 ± 110	26 ± 2
58	204.228 39	−29.926 435	22 ± 2	9 ± 1	287 ± 20	1120 ± 170	700 ± 190	370 ± 110	10 ± 0.7
59	204.179 16	−29.878 426	25 ± 3	9 ± 2	311 ± 42	1380 ± 240	890 ± 240	500 ± 110	36 ± 3
60	204.214 23	−29.871 364	20 ± 4	15 ± 4	296 ± 66	800 ± 330	860 ± 340	–	–
61	204.264 19	−29.850 760	17 ± 4	20 ± 7	515 ± 90	1050 ± 570	710 ± 340	220 ± 170	51 ± 3
62	204.262 17	−29.847 377	20 ± 5	18 ± 6	432 ± 88	1230 ± 560	640 ± 340	190 ± 150	86 ± 6
63	204.301 13	−29.838 620	15 ± 3	9 ± 1	265 ± 40	800 ± 280	640 ± 240	350 ± 170	14 ± 2
64	204.212 81	−29.835 625	24 ± 3	16 ± 2	365 ± 45	890 ± 200	540 ± 260	310 ± 160	46 ± 2
65	204.234 65	−29.825 908	14 ± 3	6 ± 4	201 ± 50	800 ± 240	670 ± 310	250 ± 170	17 ± 2
66	204.274 51	−29.895 053	24 ± 6	11 ± 3	423 ± 62	1180 ± 260	820 ± 260	330 ± 180	35 ± 2
67	204.207 33	−29.869 728	17 ± 4	13 ± 4	387 ± 68	450 ± 240	570 ± 240	200 ± 150	26 ± 4
68	204.283 85	−29.911 307	9 ± 2	6 ± 1	194 ± 20	390 ± 110	290 ± 140	150 ± 120	5 ± 2
69	204.278 82	−29.887 547	23 ± 6	11 ± 3	290 ± 49	1590 ± 270	1480 ± 360	690 ± 220	26 ± 2
70	204.299 93	−29.850 675	10 ± 3	8 ± 2	195 ± 39	410 ± 270	330 ± 270	180 ± 150	25 ± 2
71	204.212 30	−29.881 552	19 ± 4	7 ± 5	285 ± 70	1200 ± 280	740 ± 300	300 ± 190	4 ± 3
72	204.222 76	−29.853 089	21 ± 4	24 ± 7	407 ± 74	1360 ± 380	750 ± 380	440 ± 190	12 ± 3
73	204.213 39	−29.841 575	18 ± 3	26 ± 4	308 ± 46	530 ± 220	700 ± 320	170 ± 140	30 ± 2
74	204.296 38	−29.826 215	11 ± 4	7 ± 2	157 ± 40	570 ± 270	480 ± 180	300 ± 140	9 ± 4
75	204.243 62	−29.804 870	14 ± 3	9 ± 2	215 ± 30	680 ± 160	530 ± 200	350 ± 140	23 ± 2
76	204.285 00	−29.866 274	12 ± 4	16 ± 3	271 ± 49	1180 ± 330	680 ± 350	300 ± 190	19 ± 2
77	204.304 24	−29.860 591	12 ± 2	5 ± 1	185 ± 28	750 ± 200	600 ± 260	220 ± 150	14 ± 1
78	204.288 76	−29.852 195	13 ± 3	4 ± 3	286 ± 49	890 ± 280	320 ± 300	–	16 ± 3
79	204.289 07	−29.846 556	12 ± 2	6 ± 3	161 ± 33	480 ± 260	560 ± 350	–	20 ± 3
80	204.191 44	−29.880 882	10 ± 2	5 ± 1	135 ± 20	530 ± 190	480 ± 200	330 ± 120	3 ± 2
81	204.322 04	−29.864 861	10 ± 1	4.6 ± 0.8	110 ± 12	410 ± 150	230 ± 150	110 ± 72	9 ± 1
82	204.206 39	−29.859 928	14 ± 4	13 ± 3	224 ± 47	570 ± 270	350 ± 290	430 ± 170	16 ± 3
83	204.196 82	−29.818 118	15 ± 1	8.5 ± 0.7	146 ± 12	584 ± 92	340 ± 120	180 ± 73	12.8 ± 0.5
84	204.296 86	−29.926 976	16 ± 2	13 ± 1	95 ± 11	400 ± 120	290 ± 130	145 ± 81	21 ± 1
85	204.290 44	−29.908 584	10 ± 2	7 ± 0.8	94 ± 14	309 ± 93	310 ± 140	220 ± 130	3 ± 1
86	204.241 01	−29.839 948	10 ± 4	5 ± 2	113 ± 35	840 ± 260	660 ± 370	340 ± 180	34 ± 2
87	204.273 53	−29.917 803	18 ± 2	12 ± 2	207 ± 30	840 ± 170	570 ± 180	260 ± 120	60 ± 3
88	204.231 22	−29.914 030	8 ± 1	3.4 ± 0.7	96 ± 14	540 ± 170	220 ± 160	–	5.5 ± 0.7
89	204.231 79	−29.802 769	13 ± 3	3 ± 1	134 ± 29	550 ± 180	390 ± 140	400 ± 120	2 ± 2
90	204.203 38	−29.873 538	11 ± 4	30 ± 4	148 ± 57	1050 ± 260	530 ± 250	190 ± 150	9 ± 3

Table D2. HB measurement SED fitting parameters.

	χ_{UV}	χ_{col}	T_{dust} (K)	M_{dust} (10^4 M$_\odot$)	F_{24}	L_{dust} (10^{40} erg s^{-1})	χ^2_{FIT}
1	1.3 ± 0.7	9 ± 2	22.9 ± 0.8	16 ± 5	0.8 ± 0.2	47 ± 1	0.6
2	0.3 ± 0.1	9 ± 1	19.6 ± 0.1	18 ± 3	0.9 ± 0.1	28.7 ± 0.6	5.0
3	1.4 ± 0.6	6 ± 2	22.0 ± 0.6	20 ± 5	0.9 ± 0.2	45 ± 2	1.2
4	2 ± 1	8 ± 3	24 ± 1	12 ± 5	0.7 ± 0.2	35 ± 2	2.0
5	2 ± 1	4. ± 1	23.6 ± 0.7	14 ± 3	0.4 ± 0.2	32 ± 2	1.0
6	3 ± 2	6 ± 2	26 ± 1	7 ± 3	0.6 ± 0.1	31 ± 1	0.6
7	7 ± 4	8 ± 3	31 ± 3	2 ± 1	0.6 ± 0.2	24 ± 1	1.1
8	1.3 ± 0.7	9 ± 1	23.1 ± 0.6	11 ± 4	0.8 ± 0.2	25 ± 1	6.6
9	2 ± 1	6 ± 3	22.9 ± 0.7	30 ± 10	0.6 ± 0.1	52 ± 2	4.5
10	2 ± 1	2 ± 1	21 ± 1	22 ± 9	0.7 ± 0.2	35 ± 1	2.5
11	1.4 ± 0.6	6 ± 2	21.8 ± 0.4	14 ± 3	0.7 ± 0.2	23 ± 1	0.5
12	1.4 ± 0.6	8 ± 2	22.6 ± 0.4	22 ± 6	0.6 ± 0.1	40.6 ± 0.9	0.4

Table D2 – *continued*

	$\chi_{\rm UV}$	$\chi_{\rm col}$	$T_{\rm dust}$ (K)	$M_{\rm dust}$ ($10^4\,{\rm M}_\odot$)	F_{24}	$L_{\rm dust}$ (10^{40} erg s^{-1})	$\chi^2_{\rm FIT}$
13	3 ± 2	3 ± 2	23.2 ± 0.3	12 ± 3	0.4 ± 0.1	27.1 ± 0.8	0.4
14	0.6 ± 0.2	9 ± 2	21.6 ± 0.6	27 ± 8	0.5 ± 0.2	31 ± 2	1.9
15	0.4 ± 0.3	6 ± 4	18.2 ± 0.8	30 ± 10	0.7 ± 0.2	14.2 ± 0.8	2.3
16	1.4 ± 0.6	6 ± 2	21.6 ± 0.2	39 ± 7	0.8 ± 0.1	74.1 ± 0.5	2.9
17	2 ± 1	$3. \pm 1$	22.9 ± 0.7	4.4 ± 0.8	0.6 ± 0.1	10.3 ± 0.3	0.9
18	0.3 ± 0.2	9 ± 2	20 ± 1	13 ± 6	0.9 ± 0.1	14.6 ± 0.8	1.5
19	1.2 ± 0.8	7 ± 3	22 ± 1	8 ± 4	0.7 ± 0.3	12 ± 1	5.8
20	1.3 ± 0.8	7 ± 3	21.6 ± 0.7	13 ± 4	0.6 ± 0.2	16.2 ± 0.8	0.2
21	0.5 ± 0.2	9 ± 2	20.8 ± 0.5	17 ± 4	0.6 ± 0.2	17 ± 1	1.7
22	2 ± 1	4 ± 2	23.3 ± 0.3	8 ± 2	0.4 ± 0.2	18 ± 1	0.9
23	2 ± 2	6 ± 4	23 ± 2	5 ± 3	0.4 ± 0.4	7 ± 1	1.8
24	1.3 ± 0.7	3 ± 2	19.9 ± 0.4	20 ± 5	0.13 ± 0.1	12.9 ± 0.8	0.9
25	3 ± 2	4 ± 2	23.7 ± 0.7	14 ± 4	0.5 ± 0.1	37 ± 1	1.3
26	1.0 ± 1.0	7 ± 4	20 ± 2	9 ± 6	0.8 ± 0.2	10 ± 1	5.4
27	6 ± 4	5 ± 3	29 ± 3	1.5 ± 1.0	0.5 ± 0.2	8.8 ± 0.8	0.6
28	1.4 ± 0.6	4 ± 2	20.8 ± 0.4	12 ± 3	0.13 ± 0.1	10.6 ± 0.5	0.7
29	0.5 ± 0.3	8 ± 3	20.2 ± 0.8	9 ± 4	0.7 ± 0.2	7.8 ± 0.6	1.1
30	0.6 ± 0.4	7 ± 4	20 ± 1	6 ± 3	0.9 ± 0.2	6.6 ± 0.5	1.4
31	3 ± 2	1.2 ± 0.9	22 ± 1	9 ± 4	0.4 ± 0.2	17 ± 1	1.4
32	3 ± 3	7 ± 4	26 ± 2	2 ± 1	0.5 ± 0.3	6.8 ± 0.7	0.6
33	1.2 ± 0.8	7 ± 3	21.5 ± 0.8	5 ± 2	0.6 ± 0.2	5.9 ± 0.4	2.3
34	0.6 ± 0.4	8 ± 3	21 ± 1	8 ± 4	0.6 ± 0.2	7.3 ± 0.7	0.5
35	0.2 ± 0.1	8 ± 2	18 ± 1	20 ± 10	0.6 ± 0.3	7.5 ± 0.6	4.5
36	3 ± 2	3 ± 2	22.8 ± 0.7	9 ± 3	0.4 ± 0.1	17.9 ± 0.6	1.3
37	0.3 ± 0.1	9 ± 1	19.6 ± 0.1	14 ± 3	0.5 ± 0.3	9.1 ± 0.5	4.0
38	1.2 ± 0.8	7 ± 3	21.6 ± 0.7	16 ± 6	0.6 ± 0.2	21 ± 1	0.9
39	6 ± 5	3 ± 3	25 ± 3	2 ± 2	0.5 ± 0.4	7 ± 1	0.8
40	2 ± 1	4 ± 2	22 ± 1	6 ± 3	0.3 ± 0.2	7.2 ± 0.5	0.6
41	2 ± 1	3 ± 2	21.3 ± 0.8	6 ± 3	0.3 ± 0.1	7.2 ± 0.6	0.9
42	1.2 ± 0.9	7 ± 3	22 ± 2	4 ± 3	0.7 ± 0.3	6.0 ± 0.7	1.4
43	2 ± 1	6 ± 2	24.7 ± 0.5	5 ± 1	0.4 ± 0.2	14.1 ± 0.6	0.4
44	0.3 ± 0.2	9 ± 2	18.9 ± 0.8	13 ± 6	0.8 ± 0.3	7.5 ± 0.8	1.6
45	8 ± 3	2 ± 1	27 ± 1	8 ± 3	0.16 ± 0.1	48 ± 2	2.9
46	0.5 ± 0.3	8 ± 2	20.7 ± 0.9	12 ± 5	0.5 ± 0.4	9.0 ± 0.8	0.4
47	0.6 ± 0.3	9 ± 1	21.5 ± 0.9	15 ± 6	0.11 ± 0.1	13.6 ± 0.9	2.1
48	0.5 ± 0.2	4 ± 2	18.2 ± 0.3	25 ± 6	0.04 ± 0.03	9.8 ± 0.3	3.9
49	0.6 ± 0.3	5 ± 2	19.9 ± 0.6	14 ± 5	0.41 ± 0.1	9.6 ± 0.5	0.1
50	4 ± 2	0.5 ± 0.4	22.1 ± 0.7	10 ± 3	0.05 ± 0.04	17 ± 1	4.4
51	0.55 ± 0.1	6 ± 2	20.03 ± 0.06	15 ± 2	0.3 ± 0.2	10.7 ± 0.3	0.6
52	2 ± 1	2 ± 1	22.1 ± 0.7	7 ± 1	0.43 ± 0.1	13.3 ± 0.5	1.1
53	2 ± 1	3 ± 2	21 ± 1	4 ± 2	0.5 ± 0.2	4.8 ± 0.4	4.3
54	4 ± 3	6 ± 5	23 ± 3	5 ± 4	0.6 ± 0.4	6 ± 1	0.2
55	2 ± 1	7 ± 4	23 ± 1	6 ± 3	0.3 ± 0.3	10 ± 1	0.6
56	2 ± 1	$3. \pm 1$	22.9 ± 0.7	6.9 ± 0.9	0.21 ± 0.08	12.9 ± 0.2	1.0
57	1.2 ± 0.9	7 ± 3	22 ± 2	3 ± 2	0.6 ± 0.3	3.9 ± 0.5	2.9
58	0.5 ± 0.2	7 ± 2	19.8 ± 0.2	12 ± 2	0.03 ± 0.02	7.45 ± 0.04	3.1
59	0.4 ± 0.2	7 ± 3	19.2 ± 0.4	19 ± 6	0.06 ± 0.05	9.0 ± 0.5	2.0
60	1.2 ± 0.9	5 ± 3	20 ± 1	9 ± 4	0.4 ± 0.4	7.1 ± 1.0	1.5
61	1.2 ± 0.9	8 ± 2	22 ± 2	8 ± 5	0.5 ± 0.4	9 ± 1	0.3
62	1.2 ± 0.9	7 ± 4	22 ± 1	8 ± 4	0.5 ± 0.4	9 ± 1	0.4
63	0.5 ± 0.3	8 ± 3	20.1 ± 0.9	10 ± 4	0.2 ± 0.2	6.4 ± 0.6	0.5
64	1.3 ± 0.7	5 ± 2	21.1 ± 0.6	8 ± 2	0.3 ± 0.2	8.1 ± 0.6	0.6
65	0.5 ± 0.4	7 ± 3	19 ± 1	12 ± 7	0.3 ± 0.3	5.5 ± 0.8	0.5
66	0.6 ± 0.4	7 ± 3	21.1 ± 0.8	11 ± 4	0.14 ± 0.1	9.1 ± 0.8	0.8
67	3 ± 2	6 ± 4	24 ± 2	4 ± 2	0.4 ± 0.4	6.5 ± 0.9	2.2
68	1.2 ± 0.8	7 ± 3	21.8 ± 0.8	3 ± 1	0.3 ± 0.3	3.7 ± 0.4	0.7
69	0.20 ± 0.1	8 ± 2	18.1 ± 0.4	33 ± 8	0.12 ± 0.1	10.2 ± 0.7	1.0
70	2 ± 1	6 ± 4	22 ± 2	5 ± 4	0.4 ± 0.4	4.1 ± 0.7	0.3
71	0.5 ± 0.3	7 ± 3	19.7 ± 0.9	13 ± 6	0.2 ± 0.2	7.6 ± 0.8	0.5
72	0.4 ± 0.3	7 ± 3	19 ± 1	17 ± 8	0.6 ± 0.4	10 ± 1	0.1
73	2 ± 1	3 ± 3	20 ± 2	8 ± 5	0.8 ± 0.2	7.0 ± 0.6	1.5
74	0.4 ± 0.3	7 ± 4	19 ± 1	11 ± 6	0.4 ± 0.4	4.6 ± 0.7	0.5
75	0.6 ± 0.4	7 ± 4	19.7 ± 0.9	9 ± 4	0.3 ± 0.3	5.5 ± 0.5	1.3

Table D2 – *continued*

	$\chi_{\rm UV}$	$\chi_{\rm col}$	$T_{\rm dust}$ (K)	$M_{\rm dust}$ (10^4 M$_\odot$)	F_{24}	$L_{\rm dust}$ (10^{40} erg s^{-1})	$\chi^2_{\rm FIT}$
76	0.3 ± 0.2	8 ± 2	18.9 ± 0.8	15 ± 6	0.6 ± 0.3	7.2 ± 0.7	0.7
77	0.4 ± 0.2	8 ± 3	19.6 ± 0.8	9 ± 4	0.09 ± 0.08	4.9 ± 0.5	0.8
78	1.2 ± 0.9	8 ± 2	22 ± 1	6 ± 3	0.12 ± 0.1	5.3 ± 0.6	2.0
79	1.1 ± 0.9	6 ± 4	20 ± 1	7 ± 4	0.3 ± 0.3	4.0 ± 0.7	0.6
80	0.3 ± 0.2	7 ± 3	18.8 ± 0.8	10 ± 4	0.2 ± 0.2	4.1 ± 0.5	1.6
81	1.3 ± 0.8	4 ± 2	20.1 ± 0.5	4 ± 2	0.10 ± 0.09	3.0 ± 0.2	0.2
82	1.0 ± 1.0	6 ± 4	19 ± 2	10 ± 7	0.5 ± 0.3	5.6 ± 0.8	2.0
83	1.3 ± 0.8	3 ± 2	19.5 ± 0.4	7 ± 2	0.21 ± 0.1	4.3 ± 0.2	0.5
84	0.6 ± 0.4	0.4 ± 0.3	16 ± 1	12 ± 6	0.6 ± 0.2	3.7 ± 0.2	0.9
85	1.2 ± 0.9	3 ± 2	19 ± 1	6 ± 3	0.4 ± 0.2	2.8 ± 0.3	1.3
86	0.3 ± 0.2	7 ± 3	17 ± 1	20 ± 10	0.2 ± 0.2	4.5 ± 0.8	0.5
87	0.6 ± 0.3	4 ± 2	19.2 ± 0.7	11 ± 4	0.3 ± 0.2	6.1 ± 0.4	0.1
88	1.2 ± 0.9	5 ± 3	19.9 ± 1.0	4 ± 2	0.07 ± 0.06	2.5 ± 0.3	2.8
89	0.4 ± 0.3	7 ± 4	18.6 ± 0.9	11 ± 5	0.06 ± 0.05	4.0 ± 0.4	6.3
90	0.20 ± 0.1	6 ± 4	16 ± 1	20 ± 10	0.8 ± 0.2	6.6 ± 0.7	6.6

Table D3. LB measurement source fluxes and positions.

	RA (°)	δ (°)	$F_{8\,\mu\rm m}$ (mJy)	$F_{24\,\mu\rm m}$ (mJy)	$F_{70\,\mu\rm m}$ (mJy)	$F_{160\,\mu\rm m}$ (mJy)	$F_{250\,\mu\rm m}$ (mJy)	$F_{350\,\mu\rm m}$ (mJy)	F(Hα) (μJy)
1	204.278 67	−29.826 725	132 ± 9.0	302 ± 17	3.17 ± 0.17	5.43 ± 0.55	2.63 ± 0.67	1.37 ± 0.34	70 ± 7.1
2	204.264 33	−29.900 421	63 ± 6.9	197 ± 12	1.69 ± 0.11	2.59 ± 0.40	1.36 ± 0.54	0.49 ± 0.32	52 ± 2.2
3	204.221 28	−29.858 999	163 ± 12	283 ± 18	3.18 ± 0.20	5.03 ± 0.84	2.25 ± 0.72	0.70 ± 0.33	133 ± 3.2
4	204.282 71	−29.854 724	$114 \pm 10.$	166 ± 11	2.48 ± 0.16	4.40 ± 0.67	1.93 ± 0.72	0.87 ± 0.35	83 ± 3.7
5	204.231 87	−29.830 846	$142 \pm 10.$	127 ± 8.7	2.41 ± 0.15	4.04 ± 0.49	1.70 ± 0.57	0.65 ± 0.28	106 ± 3.9
6	204.226 52	−29.884 745	126 ± 9.8	192 ± 14	2.49 ± 0.17	2.93 ± 0.71	1.26 ± 0.58	0.48 ± 0.31	205 ± 3.6
7	204.228 94	−29.885 796	84 ± 8.3	144 ± 12	2.32 ± 0.17	1.87 ± 0.68	0.87 ± 0.59	–	131 ± 2.9
8	204.221 72	−29.882 527	65 ± 7.6	146 ± 11	2.08 ± 0.15	3.38 ± 0.65	2.64 ± 0.80	1.34 ± 0.37	79 ± 3.1
9	204.219 30	−29.863 860	268 ± 17	386 ± 25	4.94 ± 0.31	7.7 ± 1.2	2.60 ± 0.83	1.57 ± 0.44	238 ± 3.7
10	204.220 46	−29.880 233	175 ± 14	264 ± 19	2.29 ± 0.15	5.24 ± 0.80	3.18 ± 0.85	1.34 ± 0.37	153 ± 3.7
11	204.219 71	−29.852 660	93 ± 8.5	106 ± 11	1.56 ± 0.13	3.21 ± 0.51	1.54 ± 0.69	0.42 ± 0.31	91 ± 3.6
12	204.269 57	−29.849 437	159 ± 13	190 ± 13	3.09 ± 0.21	5.41 ± 0.98	2.16 ± 0.87	1.05 ± 0.40	210 ± 3.7
13	204.284 87	−29.869 891	144 ± 13	125 ± 9.6	1.79 ± 0.13	3.34 ± 0.54	1.37 ± 0.67	0.46 ± 0.31	101 ± 3.1
14	204.228 00	−29.882 334	116 ± 9.4	132 ± 11	2.17 ± 0.16	4.14 ± 0.86	3.37 ± 0.80	1.27 ± 0.40	34 ± 2.5
15	204.286 34	−29.858 535	70 ± 8.4	106 ± 11	0.796 ± 0.080	2.93 ± 0.52	1.26 ± 0.67	0.69 ± 0.33	20 ± 3.6
16	204.280 83	−29.852 275	260 ± 20	422 ± 32	5.04 ± 0.34	8.1 ± 1.1	5.5 ± 1.4	1.92 ± 0.46	193 ± 4.5
17	204.168 14	−29.855 863	47 ± 2.9	48 ± 3.0	0.665 ± 0.037	1.39 ± 0.19	0.85 ± 0.22	0.45 ± 0.12	62 ± 0.93
18	204.225 54	−29.844 806	51 ± 5.8	93 ± 7.2	0.918 ± 0.085	2.19 ± 0.45	0.73 ± 0.62	–	83 ± 3.2
19	204.214 63	−29.883 342	58 ± 7.4	91 ± 9.7	1.06 ± 0.11	1.70 ± 0.42	2.07 ± 0.73	0.82 ± 0.32	55 ± 3.6
20	204.283 97	−29.881 946	91 ± 10.0	76 ± 7.8	1.200 ± 0.10	2.47 ± 0.44	1.11 ± 0.60	0.31 ± 0.29	76 ± 3.7
21	204.208 49	−29.878 634	77 ± 8.1	79 ± 7.3	1.21 ± 0.12	3.75 ± 0.52	2.03 ± 0.74	1.14 ± 0.36	47 ± 4.1
22	204.269 97	−29.823 576	97 ± 9.1	81 ± 8.0	1.39 ± 0.12	3.10 ± 0.45	1.94 ± 0.62	0.78 ± 0.28	135 ± 7.3
23	204.291 86	−29.858 028	42 ± 5.9	38 ± 7.0	0.619 ± 0.076	1.00 ± 0.40	0.93 ± 0.65	0.51 ± 0.33	98 ± 4.7
24	204.252 44	−29.905 010	66 ± 9.6	40 ± 4.0	0.606 ± 0.072	1.62 ± 0.35	0.86 ± 0.48	0.29 ± 0.29	54 ± 2.3
25	204.212 23	−29.844 608	186 ± 12	165 ± 11	2.82 ± 0.18	5.53 ± 0.58	2.50 ± 0.61	1.37 ± 0.33	184 ± 4.1
26	204.218 77	−29.863 393	74 ± 7.2	147 ± 13	1.36 ± 0.13	2.17 ± 0.74	1.96 ± 0.72	–	155 ± 2.8
27	204.288 31	−29.849 784	50 ± 5.9	51 ± 7.4	0.849 ± 0.085	0.97 ± 0.40	0.80 ± 0.60	0.65 ± 0.30	67 ± 4.2
28	204.246 29	−29.907 226	38 ± 6.5	26 ± 3.3	0.474 ± 0.071	0.93 ± 0.32	0.47 ± 0.45	–	49 ± 2.3
29	204.188 35	−29.879 014	32 ± 3.9	32 ± 2.6	0.473 ± 0.045	1.21 ± 0.30	0.83 ± 0.46	0.23 ± 0.19	104 ± 3.5
30	204.180 91	−29.872 982	22 ± 3.8	41 ± 3.6	0.459 ± 0.049	0.75 ± 0.28	0.72 ± 0.42	–	71 ± 4.5
31	204.231 24	−29.845 585	117 ± 11	105 ± 8.6	1.066 ± 0.092	2.37 ± 0.56	0.78 ± 0.59	0.31 ± 0.30	29 ± 2.5
32	204.291 58	−29.819 528	31 ± 4.6	32 ± 3.1	0.620 ± 0.070	1.25 ± 0.31	0.93 ± 0.25	0.81 ± 0.21	109 ± 4.3
33	204.223 54	−29.813 422	20 ± 3.3	22 ± 2.2	0.328 ± 0.036	0.63 ± 0.23	0.48 ± 0.39	0.28 ± 0.23	19 ± 2.8
34	204.297 32	−29.831 076	49 ± 5.3	40 ± 3.3	0.709 ± 0.063	2.64 ± 0.39	2.04 ± 0.42	1.12 ± 0.27	76 ± 3.3
35	204.277 95	−29.823 031	36 ± 4.8	51 ± 6.0	0.518 ± 0.063	3.38 ± 0.45	1.79 ± 0.57	0.95 ± 0.30	18 ± 7.1
36	204.248 19	−29.810 471	84 ± 9.8	67 ± 5.0	1.110 ± 0.086	2.30 ± 0.37	1.14 ± 0.50	0.42 ± 0.21	87 ± 7.0
37	204.267 38	−29.899 060	38 ± 5.8	46 ± 5.7	0.586 ± 0.069	1.80 ± 0.40	0.91 ± 0.50	–	84 ± 2.0
38	204.236 65	−29.880 081	102 ± 12	106 ± 8.4	1.69 ± 0.16	4.3 ± 1.0	2.56 ± 0.70	1.03 ± 0.38	36 ± 2.4

Table D3 – *continued*

	RA (°)	δ (°)	$F_{8\,\mu m}$ (mJy)	$F_{24\,\mu m}$ (mJy)	$F_{70\,\mu m}$ (mJy)	$F_{160\,\mu m}$ (mJy)	$F_{250\,\mu m}$ (mJy)	$F_{350\,\mu m}$ (mJy)	$F(H\alpha)$ (μJy)
39	204.211 63	−29.866 269	42 ± 6.8	39 ± 6.3	0.616 ± 0.096	1.59 ± 0.38	1.42 ± 0.54	0.72 ± 0.29	42 ± 4.3
40	204.311 40	−29.843 049	46 ± 4.3	29 ± 2.3	0.458 ± 0.041	1.92 ± 0.32	1.15 ± 0.29	0.68 ± 0.19	42 ± 15
41	204.258 32	−29.925 232	42 ± 3.7	30 ± 2.2	0.447 ± 0.032	1.27 ± 0.23	0.72 ± 0.25	0.39 ± 0.16	66 ± 1.5
42	204.282 58	−29.887 080	35 ± 5.3	41 ± 4.7	0.561 ± 0.065	1.95 ± 0.32	1.11 ± 0.39	0.82 ± 0.32	46 ± 3.3
43	204.212 62	−29.876 963	86 ± 8.3	93 ± 7.8	1.64 ± 0.14	2.97 ± 0.50	1.72 ± 0.72	0.77 ± 0.29	65 ± 3.8
44	204.279 39	−29.857 758	29 ± 5.6	44 ± 6.3	0.483 ± 0.076	3.18 ± 0.72	1.25 ± 0.62	0.81 ± 0.35	35 ± 3.5
45	204.288 41	−29.857 795	321 ± 28	271 ± 26	4.76 ± 0.34	6.6 ± 1.1	1.59 ± 0.88	0.63 ± 0.34	161 ± 6.5
46	204.272 39	−29.821 631	57 ± 6.5	51 ± 6.7	0.782 ± 0.085	2.94 ± 0.44	1.79 ± 0.59	0.90 ± 0.29	130 ± 7.0
47	204.231 90	−29.881 713	69 ± 7.6	64 ± 8.1	1.22 ± 0.12	2.92 ± 0.83	1.94 ± 0.67	1.09 ± 0.38	68 ± 2.2
48	204.175 84	−29.875 390	77 ± 7.8	27 ± 3.2	0.490 ± 0.053	1.94 ± 0.33	1.24 ± 0.50	0.20 ± 0.17	22 ± 4.4
49	204.260 47	−29.832 599	46 ± 5.1	35 ± 2.9	0.446 ± 0.054	2.36 ± 0.40	1.75 ± 0.62	0.80 ± 0.31	–
50	204.263 16	−29.827 777	140 ± 15	66 ± 6.4	0.87 ± 0.11	2.59 ± 0.50	2.08 ± 0.73	0.42 ± 0.27	43 ± 3.1
51	204.267 79	−29.925 076	53 ± 4.1	38 ± 2.9	0.635 ± 0.045	2.16 ± 0.26	1.13 ± 0.29	0.49 ± 0.17	63 ± 3.3
52	204.280 75	−29.909 675	80 ± 6.2	64 ± 4.1	0.854 ± 0.057	2.38 ± 0.31	1.14 ± 0.30	0.52 ± 0.21	135 ± 3.2
53	204.320 62	−29.886 212	26 ± 2.9	19 ± 1.9	0.294 ± 0.029	0.72 ± 0.17	0.84 ± 0.31	0.35 ± 0.17	36 ± 1.1
54	204.234 95	−29.885 641	38 ± 6.8	42 ± 7.1	0.551 ± 0.088	1.33 ± 0.70	0.88 ± 0.51	0.32 ± 0.27	15 ± 2.6
55	204.285 09	−29.878 952	65 ± 8.0	41 ± 6.7	0.838 ± 0.089	1.55 ± 0.41	0.70 ± 0.63	–	61 ± 3.9
56	204.271 36	−29.804 832	51 ± 9.2	36 ± 3.6	0.753 ± 0.097	1.31 ± 0.41	0.60 ± 0.41	0.25 ± 0.16	46 ± 6.9
57	204.244 38	−29.801 254	15 ± 3.8	17 ± 2.5	0.257 ± 0.043	0.73 ± 0.26	0.86 ± 0.48	0.36 ± 0.19	18 ± 7.1
58	204.228 39	−29.926 435	37 ± 3.0	18 ± 1.5	0.385 ± 0.030	1.44 ± 0.22	0.81 ± 0.28	0.30 ± 0.16	15 ± 0.82
59	204.179 16	−29.878 426	54 ± 5.6	27 ± 3.4	0.561 ± 0.060	1.79 ± 0.35	1.04 ± 0.48	0.25 ± 0.19	139 ± 3.6
60	204.214 23	−29.871 364	40 ± 6.1	31 ± 5.4	0.440 ± 0.082	1.58 ± 0.48	1.52 ± 0.68	0.43 ± 0.29	–
61	204.264 19	−29.850 760	53 ± 6.9	66 ± 9.3	1.01 ± 0.12	2.89 ± 0.82	1.13 ± 0.76	0.71 ± 0.37	98 ± 4.0
62	204.262 17	−29.847 377	53 ± 7.6	48 ± 7.5	0.79 ± 0.12	1.75 ± 0.73	0.80 ± 0.78	0.37 ± 0.30	175 ± 6.1
63	204.301 13	−29.838 620	47 ± 4.4	28 ± 2.3	0.514 ± 0.052	2.46 ± 0.39	2.09 ± 0.44	1.18 ± 0.28	39 ± 2.0
64	204.212 81	−29.835 625	54 ± 5.1	33 ± 3.1	0.585 ± 0.058	1.80 ± 0.29	1.07 ± 0.40	0.60 ± 0.23	61 ± 3.2
65	204.234 65	−29.825 908	35 ± 4.9	20 ± 4.4	0.369 ± 0.064	1.31 ± 0.33	0.89 ± 0.48	0.27 ± 0.24	–
66	204.274 51	−29.895 053	46 ± 9.2	22 ± 4.1	0.54 ± 0.11	1.32 ± 0.42	0.84 ± 0.54	–	49 ± 2.0
67	204.207 33	−29.869 728	40 ± 6.3	32 ± 4.9	0.651 ± 0.087	1.57 ± 0.39	1.36 ± 0.50	0.73 ± 0.29	60 ± 4.2
68	204.283 85	−29.911 307	22 ± 2.7	17 ± 1.7	0.296 ± 0.026	1.05 ± 0.17	0.84 ± 0.27	0.43 ± 0.19	11 ± 1.8
69	204.278 82	−29.887 547	72 ± 10.	28 ± 6.5	0.441 ± 0.069	2.16 ± 0.44	1.62 ± 0.66	0.61 ± 0.32	116 ± 2.9
70	204.299 93	−29.850 675	38 ± 4.3	20 ± 2.5	0.399 ± 0.050	1.80 ± 0.36	2.00 ± 0.50	1.05 ± 0.27	44 ± 2.4
71	204.212 30	−29.881 552	64 ± 7.5	48 ± 7.0	0.699 ± 0.095	2.29 ± 0.44	1.74 ± 0.71	0.78 ± 0.32	42 ± 3.5
72	204.222 76	−29.853 089	57 ± 6.5	65 ± 9.1	0.750 ± 0.099	2.44 ± 0.54	1.06 ± 0.63	0.43 ± 0.31	15 ± 3.2
73	204.213 39	−29.841 575	61 ± 5.2	63 ± 5.2	0.685 ± 0.065	2.01 ± 0.33	1.63 ± 0.51	0.65 ± 0.23	74 ± 3.4
74	204.296 38	−29.826 215	35 ± 5.1	22 ± 3.0	0.346 ± 0.050	1.78 ± 0.35	1.39 ± 0.32	1.18 ± 0.27	29 ± 3.7
75	204.243 62	−29.804 870	32 ± 5.3	21 ± 3.1	0.346 ± 0.051	1.34 ± 0.29	1.16 ± 0.52	0.57 ± 0.22	36 ± 7.0
76	204.285 00	−29.866 274	38 ± 5.7	45 ± 7.2	0.549 ± 0.075	2.46 ± 0.52	0.87 ± 0.66	0.34 ± 0.30	52 ± 2.5
77	204.304 24	−29.860 591	32 ± 3.4	15 ± 2.0	0.325 ± 0.038	1.80 ± 0.30	1.59 ± 0.45	0.77 ± 0.25	22 ± 1.4
78	204.288 76	−29.852 195	32 ± 5.0	23 ± 5.8	0.503 ± 0.070	1.52 ± 0.43	0.74 ± 0.59	0.63 ± 0.30	68 ± 3.5
79	204.289 07	−29.846 556	29 ± 4.3	19 ± 5.8	0.306 ± 0.053	0.74 ± 0.39	0.97 ± 0.66	0.60 ± 0.30	87 ± 3.7
80	204.191 44	−29.880 882	23 ± 3.6	14 ± 1.9	0.221 ± 0.032	0.94 ± 0.29	0.77 ± 0.46	0.32 ± 0.22	12 ± 3.3
81	204.322 04	−29.864 861	24 ± 2.1	12 ± 1.1	0.200 ± 0.018	1.19 ± 0.20	0.97 ± 0.25	0.66 ± 0.14	19 ± 1.2
82	204.206 39	−29.859 928	27 ± 6.2	26 ± 4.2	0.340 ± 0.064	1.05 ± 0.39	1.20 ± 0.64	0.85 ± 0.29	34 ± 3.8
83	204.196 82	−29.818 118	26 ± 1.7	16 ± 1.1	0.225 ± 0.017	1.00 ± 0.13	0.70 ± 0.19	0.43 ± 0.12	36 ± 0.54
84	204.296 86	−29.926 976	31 ± 3.4	24 ± 1.9	0.170 ± 0.017	0.62 ± 0.17	0.44 ± 0.23	0.18 ± 0.13	39 ± 1.4
85	204.290 44	−29.908 584	22 ± 3.2	14 ± 1.6	0.133 ± 0.023	0.71 ± 0.16	0.82 ± 0.29	0.47 ± 0.20	7.5 ± 1.3
86	204.241 01	−29.839 948	37 ± 6.2	13 ± 2.8	0.239 ± 0.055	1.45 ± 0.49	0.90 ± 0.85	0.36 ± 0.34	167 ± 2.6
87	204.273 53	−29.917 803	44 ± 4.0	31 ± 2.7	0.429 ± 0.043	1.58 ± 0.25	1.05 ± 0.31	0.44 ± 0.18	190 ± 2.6
88	204.231 22	−29.914 030	18 ± 2.2	7.6 ± 1.0	0.178 ± 0.025	0.84 ± 0.22	0.35 ± 0.25	–	7.30 ± 0.75
89	204.231 79	−29.802 769	21 ± 4.7	7.1 ± 1.9	0.123 ± 0.051	0.58 ± 0.28	0.64 ± 0.39	0.36 ± 0.21	–
90	204.203 38	−29.873 538	30 ± 5.7	74 ± 7.4	0.380 ± 0.078	1.74 ± 0.39	1.15 ± 0.53	0.66 ± 0.30	25 ± 3.7

Table D4. LB measurement SED fitting parameters.

	$\chi_{\rm UV}$	$\chi_{\rm col}$	$T_{\rm dust}$ (K)	$M_{\rm dust}$ (10^4 M$_\odot$)	F_{24}	$L_{\rm dust}$ (10^{40} erg s^{-1})	$\chi^2_{\rm FIT}$
1	0.7 ± 0.3	4 ± 2	19.8 ± 0.7	40 ± 20	0.8 ± 0.2	67 ± 2	1.3
2	0.5 ± 0.3	4 ± 3	18.1 ± 1.0	30 ± 10	0.9 ± 0.1	36 ± 1	1.7
3	3 ± 2	2 ± 1	22.3 ± 0.2	20 ± 5	0.8 ± 0.1	65 ± 1	1.9
4	2 ± 1	4 ± 2	22.1 ± 0.9	30 ± 10	0.7 ± 0.1	49 ± 2	1.4
5	3 ± 1	$2. \pm 1$	23.5 ± 0.7	17 ± 2	0.40 ± 0.08	44.8 ± 0.5	1.5
6	6 ± 4	2 ± 1	25 ± 2	8 ± 5	0.8 ± 0.1	45 ± 3	0.8
7	7 ± 4	4 ± 2	28 ± 2	4 ± 2	0.7 ± 0.2	36 ± 2	0.4
8	0.5 ± 0.3	9 ± 1	20.7 ± 0.9	30 ± 10	0.8 ± 0.2	41 ± 2	2.3
9	3 ± 2	2 ± 1	22.8 ± 0.7	30 ± 10	0.8 ± 0.1	97 ± 2	2.3
10	1.3 ± 0.8	1 ± 1	18 ± 1	70 ± 30	0.7 ± 0.1	59 ± 2	1.6
11	2 ± 1	2 ± 1	22.1 ± 0.7	15 ± 2	0.6 ± 0.2	32 ± 1	1.5
12	2 ± 1	3 ± 1	22.9 ± 0.7	23 ± 4	0.6 ± 0.2	58 ± 3	1.1
13	4 ± 2	1.2 ± 0.8	23 ± 1	14 ± 5	0.5 ± 0.1	38 ± 2	1.0
14	1.3 ± 0.7	5 ± 2	20.8 ± 0.4	37 ± 9	0.7 ± 0.1	46 ± 1	1.6
15	0.5 ± 0.3	1.1 ± 0.9	16.8 ± 0.9	50 ± 20	0.7 ± 0.1	24 ± 1	4.2
16	2 ± 1	3 ± 2	21 ± 1	50 ± 20	0.8 ± 0.2	106 ± 5	2.3
17	1.5 ± 0.5	3 ± 2	20.2 ± 0.4	14 ± 3	0.61 ± 0.08	15.6 ± 0.2	2.7
18	1.2 ± 0.8	3 ± 2	19 ± 1	20 ± 8	0.9 ± 0.2	21.6 ± 0.9	2.2
19	1.2 ± 0.9	3 ± 2	19 ± 2	30 ± 10	0.8 ± 0.2	23 ± 1	2.8
20	3 ± 2	2 ± 1	22.8 ± 0.7	12 ± 5	0.4 ± 0.2	25 ± 2	1.5
21	0.6 ± 0.3	5 ± 2	19.5 ± 0.6	40 ± 20	0.5 ± 0.1	30 ± 1	0.4
22	2 ± 1	3 ± 2	21.3 ± 0.8	23 ± 8	0.5 ± 0.2	30 ± 1	1.1
23	3 ± 2	2 ± 2	22 ± 1	8 ± 5	0.5 ± 0.3	12.7 ± 0.9	1.0
24	3 ± 2	1.2 ± 0.9	21.5 ± 0.9	11 ± 4	0.2 ± 0.2	15 ± 1	0.2
25	2 ± 1	2 ± 1	22.1 ± 0.7	32 ± 4	0.45 ± 0.08	58.1 ± 0.7	1.2
26	2 ± 2	1 ± 1	20 ± 3	20 ± 10	0.9 ± 0.2	30 ± 2	3.1
27	4 ± 3	3 ± 2	24 ± 2	6 ± 3	0.6 ± 0.2	16 ± 1	2.4
28	5 ± 4	2 ± 1	24 ± 2	4 ± 3	0.3 ± 0.3	10 ± 1	0.4
29	1.3 ± 0.7	4 ± 2	20.2 ± 0.3	11 ± 3	0.6 ± 0.1	11.2 ± 0.6	0.6
30	2 ± 1	4 ± 3	20 ± 2	11 ± 8	0.9 ± 0.2	10.0 ± 0.9	0.6
31	3 ± 2	0.3 ± 0.2	21 ± 1	15 ± 6	0.5 ± 0.2	27 ± 1	1.7
32	0.6 ± 0.4	7 ± 3	20.6 ± 0.9	15 ± 6	0.5 ± 0.1	13.4 ± 0.8	4.7
33	2 ± 1	3 ± 2	21 ± 1	6 ± 4	0.6 ± 0.2	7.2 ± 0.7	0.5
34	0.4 ± 0.2	6 ± 2	18.7 ± 0.2	40 ± 10	0.4 ± 0.1	20.1 ± 0.9	1.2
35	0.15 ± 0.05	9 ± 2	16.5 ± 0.2	80 ± 20	0.7 ± 0.1	18.9 ± 0.9	4.2
36	2 ± 1	2 ± 1	22.1 ± 0.7	13 ± 2	0.45 ± 0.08	23.7 ± 0.3	0.7
37	1.2 ± 0.9	4 ± 3	20 ± 1	19 ± 9	0.7 ± 0.2	15 ± 1	1.2
38	1.3 ± 0.8	4 ± 2	20.6 ± 0.6	40 ± 10	0.57 ± 0.1	38 ± 1	0.3
39	1.2 ± 0.9	5 ± 3	20 ± 1	20 ± 10	0.5 ± 0.2	15 ± 1	1.2
40	0.55 ± 0.1	$3. \pm 1$	18.8 ± 0.3	27 ± 5	0.3 ± 0.1	14.1 ± 0.2	0.3
41	2 ± 1	2 ± 1	20.3 ± 0.8	12 ± 5	0.4 ± 0.1	11.7 ± 0.9	1.3
42	0.4 ± 0.3	6 ± 3	18.7 ± 0.6	30 ± 10	0.6 ± 0.2	15.2 ± 0.9	0.6
43	2 ± 1	4 ± 2	22.1 ± 0.9	20 ± 8	0.5 ± 0.1	32 ± 2	1.1
44	0.20 ± 0.1	8 ± 3	17.1 ± 0.9	50 ± 20	0.7 ± 0.2	16 ± 1	2.8
45	8 ± 2	1.3 ± 0.7	26.4 ± 0.8	14 ± 4	0.4 ± 0.2	83 ± 4	2.7
46	0.5 ± 0.3	5 ± 2	19.0 ± 0.6	40 ± 10	0.5 ± 0.2	22 ± 1	0.3
47	1.2 ± 0.8	5 ± 2	20.7 ± 0.7	30 ± 10	0.5 ± 0.2	28 ± 2	0.6
48	2 ± 1	1.2 ± 0.8	20.8 ± 0.3	12 ± 2	0.02 ± 0.02	14.2 ± 0.7	7.5
49	0.4 ± 0.2	4 ± 2	17.8 ± 0.1	40 ± 10	0.4 ± 0.1	15.8 ± 0.9	0.3
50	3 ± 2	0.4 ± 0.3	21.3 ± 1.0	20 ± 8	0.09 ± 0.08	26 ± 1	2.0
51	1.4 ± 0.6	3 ± 1	20.2 ± 0.3	20 ± 5	0.33 ± 0.1	16.8 ± 0.5	1.1
52	2 ± 1	1.4 ± 0.6	21.0 ± 0.1	15 ± 2	0.40 ± 0.08	21.3 ± 0.4	1.7
53	1.4 ± 0.6	2 ± 1	19.7 ± 0.2	10 ± 2	0.4 ± 0.2	7.6 ± 0.3	2.4
54	2 ± 1	3 ± 2	20 ± 2	10 ± 10	0.6 ± 0.2	13 ± 2	0.2
55	6 ± 4	2 ± 1	25 ± 1	6 ± 3	0.2 ± 0.2	16 ± 2	1.0
56	3 ± 2	3 ± 2	23.8 ± 0.9	6 ± 3	0.3 ± 0.2	$14 \pm 1.$	0.1
57	0.5 ± 0.4	7 ± 4	19 ± 1	14 ± 8	0.7 ± 0.2	6.6 ± 0.8	1.0
58	1.4 ± 0.6	$3. \pm 1$	20.2 ± 0.3	13 ± 3	0.09 ± 0.08	10.5 ± 0.3	0.9
59	2 ± 1	3 ± 2	21.3 ± 0.8	13 ± 6	0.08 ± 0.07	14 ± 1	2.3
60	1.2 ± 0.9	3 ± 2	18.9 ± 1.0	20 ± 10	0.5 ± 0.3	13 ± 1	0.6
61	1.2 ± 0.9	6 ± 3	20 ± 1	20 ± 10	0.7 ± 0.2	23 ± 2	0.5
62	2 ± 2	3 ± 2	22 ± 2	12 ± 7	0.5 ± 0.2	17 ± 2	0.1
63	0.3 ± 0.1	5 ± 1	18.1 ± 0.5	47 ± 6	0.23 ± 0.10	17.1 ± 0.3	1.2

Table D4 – *continued*

	χ_{UV}	χ_{col}	T_{dust} (K)	M_{dust} (10^4 $M_\odot$)	F_{24}	L_{dust} (10^{40} erg s^{-1})	χ^2_{FIT}
64	1.4 ± 0.6	3 ± 2	20.1 ± 0.5	20 ± 5	0.26 ± 0.1	15.7 ± 0.8	0.9
65	1.3 ± 0.8	3 ± 2	19.8 ± 0.8	15 ± 6	0.3 ± 0.3	10 ± 1	0.6
66	3 ± 2	3 ± 2	22.8 ± 0.7	6 ± 2	0.10 ± 0.09	11.3 ± 0.9	0.5
67	1.2 ± 0.8	6 ± 3	20.5 ± 0.9	17 ± 7	0.4 ± 0.3	15 ± 1	1.5
68	0.5 ± 0.3	5 ± 2	19.1 ± 0.6	16 ± 6	0.4 ± 0.2	8.2 ± 0.6	0.9
69	1.3 ± 0.8	2 ± 1	18.6 ± 0.6	30 ± 10	0.11 ± 0.1	16 ± 1	1.2
70	0.3 ± 0.2	6 ± 3	17.9 ± 0.5	40 ± 20	0.15 ± 0.1	13.7 ± 0.9	3.1
71	1.2 ± 0.8	3 ± 2	19.2 ± 0.8	30 ± 10	0.4 ± 0.2	19 ± 1	0.5
72	1.2 ± 0.8	3 ± 2	19.3 ± 0.9	30 ± 10	0.6 ± 0.2	20 ± 1	1.3
73	0.7 ± 0.3	$2. \pm 1$	18.6 ± 0.7	30 ± 10	0.6 ± 0.2	19.4 ± 0.9	0.7
74	0.3 ± 0.2	6 ± 3	17.6 ± 0.5	50 ± 10	0.3 ± 0.2	12.6 ± 0.8	2.7
75	0.6 ± 0.4	4 ± 2	19.0 ± 0.9	20 ± 10	0.3 ± 0.2	10.5 ± 0.8	0.7
76	0.5 ± 0.3	5 ± 3	18.6 ± 1.0	30 ± 10	0.7 ± 0.2	15 ± 1	2.7
77	0.3 ± 0.2	6 ± 2	18.1 ± 0.4	40 ± 10	0.07 ± 0.06	11.4 ± 0.6	1.5
78	1.2 ± 0.9	6 ± 3	20 ± 1	17 ± 8	0.4 ± 0.4	12 ± 1	0.7
79	2 ± 1	3 ± 2	20 ± 2	10 ± 10	0.4 ± 0.4	8 ± 1	1.9
80	1.2 ± 0.9	3 ± 2	19 ± 1	14 ± 7	0.3 ± 0.2	7.1 ± 0.8	0.1
81	0.3 ± 0.2	5 ± 2	17.4 ± 0.3	30 ± 10	0.10 ± 0.09	8.0 ± 0.5	2.2
82	0.4 ± 0.3	6 ± 4	17 ± 2	40 ± 30	0.6 ± 0.3	10 ± 1	2.1
83	0.7 ± 0.3	3 ± 2	18.8 ± 0.4	14 ± 4	0.27 ± 0.10	7.6 ± 0.4	1.2
84	0.6 ± 0.4	0.2 ± 0.1	17 ± 1	19 ± 9	0.5 ± 0.2	6.8 ± 0.3	2.6
85	0.4 ± 0.3	2 ± 1	16.5 ± 0.8	30 ± 10	0.4 ± 0.2	5.7 ± 0.5	1.1
86	1.2 ± 0.9	2 ± 2	18.7 ± 0.8	20 ± 10	0.07 ± 0.06	9 ± 1	1.3
87	1.3 ± 0.7	2 ± 1	19.4 ± 0.5	19 ± 6	0.36 ± 0.1	12.8 ± 0.4	0.3
88	1.2 ± 0.8	4 ± 2	19.8 ± 0.8	8 ± 3	0.07 ± 0.06	5.1 ± 0.4	1.8
89	1.1 ± 0.9	3 ± 2	18 ± 2	20 ± 10	0.10 ± 0.09	4.6 ± 0.7	1.4
90	0.2 ± 0.1	4 ± 3	14.9 ± 0.7	70 ± 30	0.9 ± 0.2	15 ± 1	7.4

This paper has been typeset from a TEX/LATEX file prepared by the author.